Flow (2025), **5** E1
doi:10.1017/flo.2024.31

FLOW CAMBRIDGE UNIVERSITY PRESS

CRITICAL REVIEW

Thermally driven cross-shore flows in stratified basins: a review on the thermal siphon dynamics

Damien Bouffard[1,2,*], Tomy Doda[1,2], Cintia L. Ramón[3] and Hugo N. Ulloa[4]

[1]Department of Surface Waters–Research and Management, Eawag, Swiss Federal Institute of Aquatic Science and Technology, Kastanienbaum, Switzerland
[2]Faculty of Geoscience and Environment, Institute of Earth Surface Dynamics, University of Lausanne, Lausanne, Switzerland
[3]Water Institute and Department of Civil Engineering, University of Granada, Granada, Spain
[4]Department of Earth and Environmental Science, University of Pennsylvania, Philadelphia, PA 19104-6316, USA
*Corresponding author. E-mail: damien.bouffard@eawag.ch

Received: 8 February 2024; **Revised:** 3 October 2024; **Accepted:** 21 October 2024

Keywords: Buoyancy flows; penetrative convection; density currents; horizontal convection; convection in cavities

Abstract

The sloping boundaries of stratified aquatic systems, such as lakes, are crucial environmental dynamic zones. While the role of sloping boundaries as energy dissipation hotspots is well established, their contribution to triggering large-scale motions has received less attention. This review delves into the development of thermally driven cross-shore flows on sloping boundaries under weak wind conditions. We specifically examine 'thermal siphons' (TS), a dynamical process that occurs when local free convection transforms into a horizontal circulation over sloping boundaries. Thermal siphons result from bathymetrically induced temperature (i.e. density) gradients when a lake experiences a uniform surface buoyancy flux, also known as differential cooling or heating. In the most common case of differential cooling of waters above the temperature of maximum density, TS lead to an overturning circulation characterised by a downslope density current and a surface return flow within a convective environment. Field observations, laboratory experiments and high-fidelity simulations of TS provide insights into their temporal occurrence, formation mechanisms, water transport dynamics and cross-shore pathways, addressing pivotal questions from an aquatic system perspective. Fluid mechanics is a fundamental tool in addressing such environmental questions and thereby serves as the central theme in this review.

Impact Statement

Lakes are often perceived as systems governed by vertical heat fluxes. This perspective stems from assuming that horizontal heterogeneities and transport have minimal impact on the vertical structure of water bodies. Nonetheless, horizontal processes can play a crucial role in mass and heat distribution in aquatic ecosystems, as evidenced by the thermohaline circulation in ocean basins. Current mechanistic models frequently overlook horizontal exchanges between shallow littoral and deep pelagic waters, constraining our understanding of the entire aquatic ecosystem. This review emphasises the underestimated role of thermally driven cross-shore flows, known as thermal siphons (TS), in facilitating horizontal exchanges. Operating daily, TS exchange waters between the littoral and pelagic zone, where vertical stratification could be already present. This process substantially influences the redistribution of water constituents between littoral and pelagic regions, shaping the biogeochemical functioning of aquatic ecosystems.

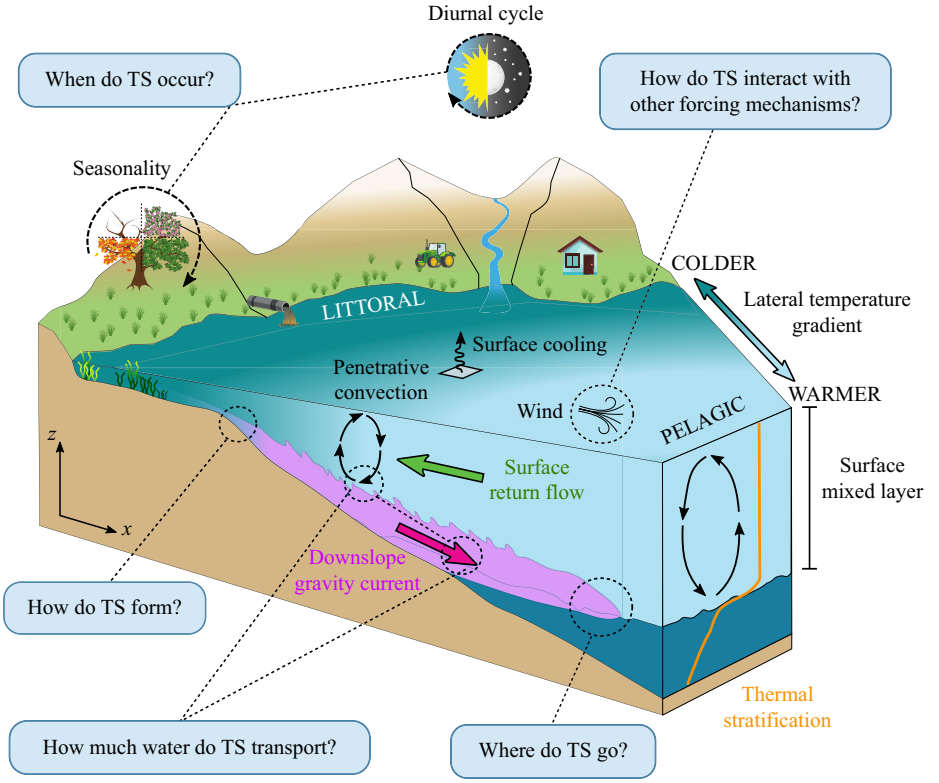

Figure 1. *Schematic of a thermal siphon (TS) driven by differential cooling for lake temperature above the temperature of maximum density, T_{md}, along with main questions that have motivated this review. Adapted from Doda (2022).*

1. Introduction from a limnology standpoint

Littoral regions of lakes are the lateral boundaries that exchange matter and energy with the surrounding watershed. They receive sediment and chemicals from the terrestrial environment, including anthropogenic contaminants. Cross-shore flows facilitate the connection and exchange between the littoral and the pelagic (away from the shore) regions. Such lateral transport controls the residence time of nearshore waters and the redistribution of heat, dissolved and particulate compounds throughout the lake. Ignoring the effects of cross-shore flows on lake physics and biogeochemistry is equivalent to representing lakes as isolated vertical water columns. This one-dimensional simplification may hold for studying trends over climate time scales. Yet, it is often insufficient when it comes to understanding short-lived processes or geographically constrained anthropogenic impacts, for which spatial heterogeneity cannot be neglected anymore (Kratz, MacIntyre & Webster 2005).

Horizontal exchange flows in lakes are driven by various mechanisms, as documented in Imberger & Patterson (1989), Wüest & Lorke (2003) and Bouffard & Wüest (2019). Early studies by pioneering limnologists unveiled that wind stands as the primary energy source propelling water movements, thereby driving horizontal transport (Wedderburn 1907; Mortimer 1953). These motions encompass a wide range of processes, not reviewed here, including surface and internal gravity waves, wind-driven cross-shore circulation, cross-shore Ekman transport in rotating environments and differential deepening of the surface mixed layer. This review focuses on weak to moderate wind forcing conditions, which allow for other processes to become discernible and impactful. Specifically, our focus lies in the creation of horizontal temperature (e.g. density) gradients, stemming from differential heating and cooling between shallow and deep waters, which ultimately drive buoyancy-induced flows (figure 1).

https://doi.org/10.1017/flo.2024.31 Published online by Cambridge University Press

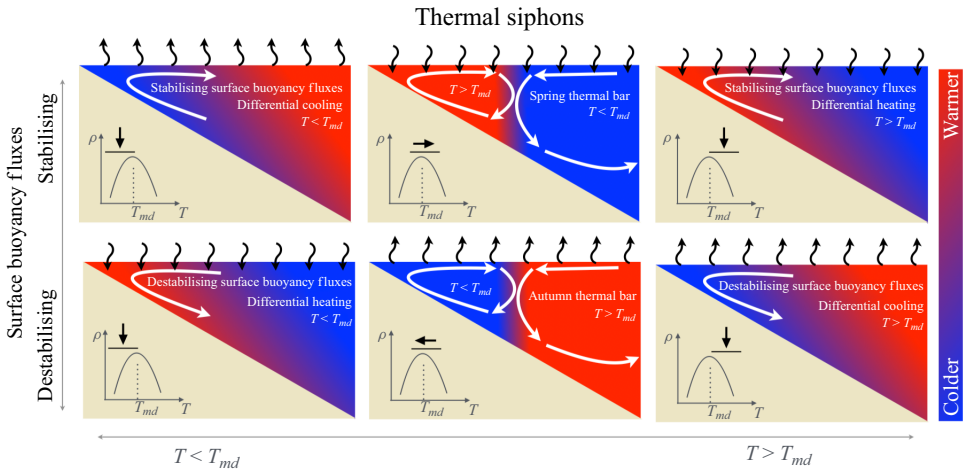

Figure 2. *Schematics showing different cases of TS with resulting circulation (white arrows) driven by stabilising and destabilising surface buoyancy fluxes, under various background temperature conditions with respect to* T_{md}.

Horizontal temperature gradients arise from spatially heterogeneous heat fluxes across the lake surface, driven by various factors such as variations in meteorological conditions, geothermal heating, shading from vegetation, wind patterns or changes in water turbidity. More ubiquitous conditions also trigger such buoyancy-driven lateral flows, when waters of varying depths experience spatially uniform heat loss or gain. The depth and therefore volume of waters in the littoral region are less than those of its offshore counterpart. Consequently, shallow littoral waters respond faster than offshore deep waters to similar stabilising or destabilising buoyancy fluxes. A stabilising buoyancy flux forces a 'gravitationally stable' local vertical density distribution. Conversely, a destabilising buoyancy flux forces a 'gravitationally unstable' local vertical density distribution. However, we stress that both buoyancy fluxes acting on sloping water bodies can set horizontal density gradients that are unconditionally unstable. The resulting horizontal density gradient can drive two types of circulation. In the case of stabilising buoyancy fluxes, we observe an upslope current with surface current directed offshore. In the case of destabilising buoyancy fluxes, we instead observe a downslope density current with a surface return current toward the shore. Such destabilising buoyancy fluxes result when surface cooling occurs on waters with temperatures above T_{md} or when solar radiation heats volumetrically waters with temperatures below T_{md} (see schematics in figure 2). These convective flows are called thermal siphons (TS), a term adopted by Monismith, Imberger & Morison (1990) who describe the development of the cross-shore circulation resulting from a bathymetrically induced temperature (and density) gradient. Given that all lakes possess sloping boundaries, TS therefore have the potential to be a ubiquitous process in lakes. Interestingly, nearshore sloping boundaries of lakes have been primarily studied for their role in dissipating mechanical energy rather than fostering cross-shore flows.

The majority of TS reported in lakes are driven by destabilising buoyancy fluxes either leading to differential cooling for $T > T_{md}$ or to differential heating for $T < T_{md}$. In contrast, TS driven by stabilising surface buoyancy fluxes are more sensitive to weak wind disturbances, which make them more difficult to observe in the natural system (Monismith *et al.* 1990; James, Barko & Eakin 1994). Therefore, we discuss field observations that primarily report TS driven by destabilising surface buoyancy fluxes.

It is worth mentioning that TS also develop in marginal seas and continental shelves. In these oceanic environments, buoyancy-driven exchange flows between the continental shelf and the deep waters emerge due to lateral density gradients controlled simultaneously by temperature and salinity conditions. Thus, dense shelf-water cascading occurs when shelf waters become denser than offshore waters because of surface cooling or salinity increase by evaporation or by ice formation (Shapiro 2003; Ivanov *et al.*

https://doi.org/10.1017/flo.2024.31 Published online by Cambridge University Press

2004). A reversed cross-shore circulation has also been observed in the case of differential heating in reef systems (Monismith *et al.* 2006; Molina *et al.* 2014) or more saline offshore waters (Lennon *et al.* 1987). Salinity-driven cross-shore flows may also occur in saline lakes, but the phenomenon requires further investigation. Here, however, we centre our discussion on the fluid dynamics of thermally driven cross-shore flows in freshwater bodies, ignoring salinity effects.

Pioneer limnological studies reported differential cooling in tropical lakes (Talling 1963; Eccles 1974). Yet, the cross-shore water transport resulting from cooling-driven TS was first quantified in reservoirs called 'cooling lakes', where warm water from power plants cools in sidearms and flows back to the main deep reservoir (Adams & Wells 1984). Monismith *et al.* (1990) provided insight into the daily cycle of differential heating/cooling phenomenon, the resulting TS and their interaction with the wind in a sidearm of a reservoir. Since this work, TS have been identified in lakes of diverse shapes and sizes, such as elongated reservoirs (James & Barko 1991*a*,*b*; James *et al.* 1994; Rogowski *et al.* 2019), small round lakes (Sturman, Oldham & Ivey 1999), wide bays (Cannaby, White & Bowyer 2007; Pálmarsson & Schladow 2008; Razlutskij *et al.* 2021), sloping sides of a large lake (Thorpe 1999; Fer, Lemmin & Thorpe 2001, 2002*b*) and various lake basins (Roget *et al.* 1993). These studies reported similar characteristics for cooling-driven TS, including the development of a near-bottom stratification along the slope, a lag between thermal forcing and flow changes, a littoral flushing time scale of a few hours and flow velocities of 0.1–10 cm s^{-1}, estimated from drogues, dye tracers and velocity time series at specific depths. More recently, Doda *et al.* (2022) explored the seasonality of cooling-driven TS in Rotsee, a wind-sheltered, small and elongated lake in Switzerland. The observations revealed that the intensity of TS was particularly pronounced from late summer to early autumn. This field-based study, devoted to characterising the occurrence and physical properties of TS, offers the most comprehensive insight into the seasonality of TS in lakes to date.

For a long time, TS have been linked to and hypothesised to sustain cross-shore transport of nutrients, pollutants, plankton, suspended sediment and dissolved gases (Stefan, Horsch & Barko 1989; Monismith *et al.* 1990; MacIntyre & Melack 1995; Fer *et al.* 2001; Pálmarsson & Schladow 2008; Doda *et al.* 2024). James & Barko (1991*a*,*b*) estimated phosphorus lateral exchange rates from phosphorus concentration gradients and TS velocity. Fer, Lemmin & Thorpe (2002*a*) attributed an increase in acoustic scattering during cooling-driven TS events to the downslope transport of suspended sediment. Cooling-driven TS have also been suggested to contribute to the renewal of deep waters (Peeters *et al.* 2003; Ambrosetti, Barbanti & Carrara 2010; Lemmin 2020; Biemond *et al.* 2021). Thermal siphons have also been hinted as the process that may explain the presence of a cold water layer above the sediment (Talling 1963; Eccles 1974; MacIntyre & Melack 1995; Wells & Sherman 2001; Woodward *et al.* 2017) and cold intrusions (Forrest *et al.* 2008) observed in certain lakes. Recently, Doda *et al.* (2024) demonstrated through a comprehensive field experiment that TS can exchange dissolved gases between littoral and pelagic regions of lakes, and effectively mobilise littoral waters at the base of the pelagic surface mixed layer.

This review addresses the questions presented in figure 1. In § 2 we introduce the concept of TS from a fundamental fluid mechanics perspective and frame the role of the equation of state, forcing mechanisms and boundary conditions to investigate the fluid physics of TS. In § 3 we differentiate the stabilising and destabilising surface buoyancy fluxes in the case $T > T_{md}$ (see also figure 2). In § 4 we review the various time scales associated with the onset and development of TS (i.e. How do TS form?). In § 5 we discuss the resulting transport associated with TS (i.e. How much water do TS transport?). Given that forcing is often temporally varying, we discuss the consequences of unsteady forcing in § 6, specifically focusing on the diurnal evolution of heat fluxes at the air–water interface and how such temporally varying forcing can help in assessing how penetrative convection modulates lateral transport. In § 7 we review the fate of the transported water mass and show the large-scale consequences of this process, particularly in ice-covered lakes where other heat and momentum sources are reduced by the presence of surface ice (i.e. Where do TS go?). In this section we also discuss the development of thermals. In § 8 we discuss the interaction between differential cooling and wind, as is often the case in

https://doi.org/10.1017/flo.2024.31 Published online by Cambridge University Press

lakes (i.e. How do TS interact with other forcing mechanisms?). Lastly, we conclude (§ 9) by outlining future research directions. Mathematical details can be found in the appendices. Although thermally driven cross-shore flows can occur in various bodies of water, this review focuses specifically on lakes. The authors consider lakes to be ideal natural field-scale laboratories for investigating fluid mechanics questions, as demonstrated in this paper.

2. Introduction from a fluid mechanics standpoint

2.1. Fundamentals of TS

Thermal siphons are a fascinating convective dynamics phenomenon. Their emergence hinges on the presence of a destabilising density gradient, which creates a pressure gradient that ultimately drives a convective flow. If we consider the fluid to be freshwater, its density and spatial gradients are determined by temperature. The action of gravity on horizontal density gradients creates buoyancy anomalies, which become a source of available potential energy that can be transformed into kinetic energy – i.e. motion (Winters *et al.* 1995; Hughes, Gayen & Griffiths 2013). Although other fluid phenomena share the above driving mechanisms, including the canonical problem of horizontal convection (Rossby 1965; Sturman, Ivey & Taylor 1996; Hughes & Griffiths 2008; Winters & Young 2009; Gayen *et al.* 2013; Griffiths, Hughes & Gayen 2013; Amber & O'Donovan 2018) and more complex problems such as the stratified horizontal convection (Noto *et al.* 2023), these phenomena result from a direct gradient of heating or cooling of the bottom or the top surface of the fluid. The case of TS is different: differential cooling or heating refers to the interplay between spatially uniform atmospheric forcing and varying bathymetry that leads to spatially varying rates of temperature change (cooling or heating).

As an analogue model for aquatic systems, we consider freshwater bodies with a horizontal surface with a normal vector parallel to the gravity field and a sloping bottom boundary, such that the systems have distinctive shallow and deep regions (figure 3). A uniform cooling of the surface, or internal heating of the body, induces a horizontal density gradient, eventually initiating an overturning flow between the shallow and deep waters. This horizontal density gradient occurs because the net heating or cooling rate in the fluid column depends on the local depth: shallower waters cool or warm faster than deep waters. Therefore, a critical element for TS development is the presence of a sloping bottom boundary, a fundamental geometric characteristic of natural aquatic systems. Table 1 provides a comprehensive overview of the key variables and parameters essential for investigating and characterising thermal siphons, along with their respective magnitudes.

2.2. Fluid properties

We focus our review on shallow freshwater systems, explicitly ignoring the effects of salt and its gradients throughout the water body. We also assume that variations in pressure are negligible in littoral regions where TS occur (e.g. compressibility effects are neglected). In this scenario, the equation of state of water, linking the fluid temperature T to its density ρ, can be characterised by a polynomial function. A reference model is provided by (Chen & Millero 1986):

$$\begin{aligned}\rho(T) = {} & 999.8395 + 6.7914 \times 10^{-2} T - 9.0894 \times 10^{-3} T^2 + 1.0171 \times 10^{-4} T^3 \\ & - 1.2846 \times 10^{-6} T^4 + 1.1592 \times 10^{-8} T^5 - 5.0125 \times 10^{-11} T^6 \ (\mathrm{kg\,m^{-3}}).\end{aligned} \tag{2.1}$$

An important fluid property for studying TS is the thermal expansivity of water:

$$\alpha = -\frac{1}{\rho}\left(\frac{\partial \rho}{\partial T}\right) (^{\circ}\mathrm{C}^{-1}). \tag{2.2}$$

https://doi.org/10.1017/flo.2024.31 Published online by Cambridge University Press

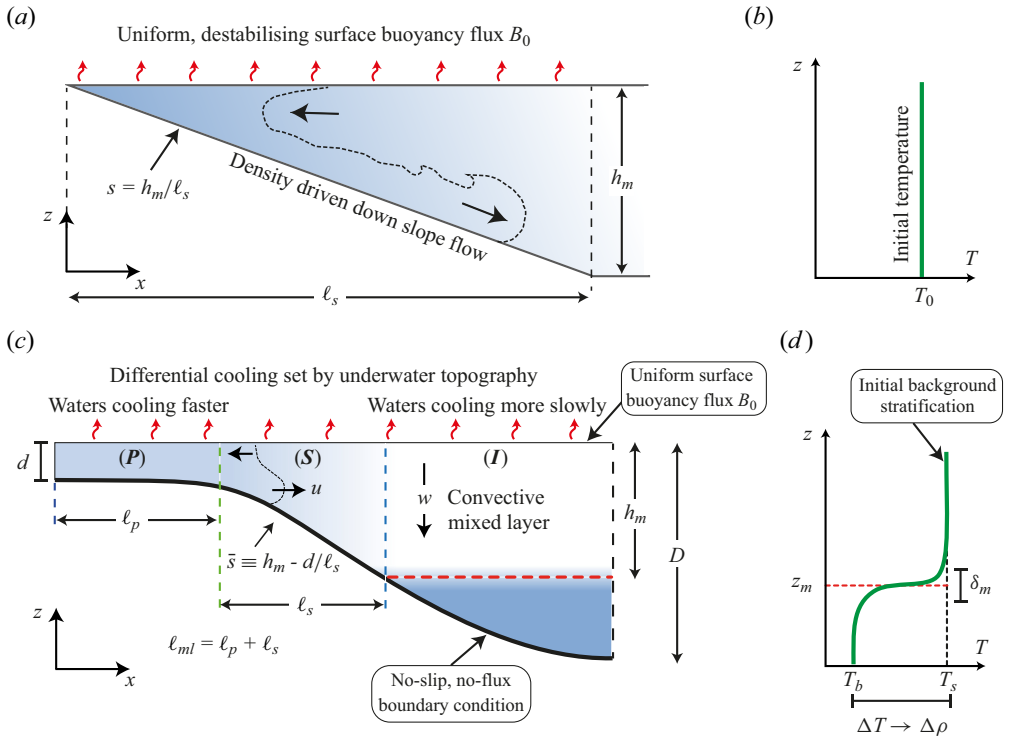

Figure 3. *(a,b) Conceptual model adopted by Horsch & Stefan (1988) and Sturman et al. (1999) for the study of convective circulation due to a destabilising surface buoyancy flux B_0 in littoral waters of characteristic slope $s = h_m/\ell_s$, the ratio of the interior surface mixed layer h_m to the horizontal length of the nearshore sloping bottom ℓ_s. (c,d) Conceptual model adopted by Wells & Sherman (2001) and Ulloa et al. (2022) for littoral regions of water basins. The system considers a shallow plateau (P) of characteristic depth d and horizontal extent ℓ_p joined through a sloping (S) bottom region of horizontal extent ℓ_s and characteristic slope $\bar{s}$ to the interior (I) stratified basin. The reference system is positive upwards with the origin at the base of the water body. The horizontal distance $\ell_{ml} = \ell_p + \ell_s$ characterises the littoral region. The initial temperature distribution is characterised by a two-layer stratification with a surface well-mixed layer of thickness h_m, a smooth metalimnion region of length δ_m and a maximum depth D. The free surface has an inhomogeneous Neumann boundary condition that models a uniform surface heat loss that sets a uniform destabilising surface buoyancy flux B_0. For both models, the solid bottom is considered adiabatic and no-slip. Colours provide a conceptual temperature distribution, with colder temperatures depicted with darker blue colours.*

This quantity can be readily determined from (2.1). The thermal expansivity α determines the magnitude of the density anomalies due to temperature differences. Lateral temperature gradients $\partial T/\partial x$ originating from differential heating or cooling create lateral density gradients $\partial \rho/\partial x = -\alpha \rho \partial T/\partial x$ that drive TS, where x is the cross-shore coordinate increasing with distance from the shore (figure 3). The maximal water density ($\alpha = 0$) is reached around $T_{md} \approx 3.98\,^{\circ}\mathrm{C}$. For systems with $T < T_{md}$ ($\alpha < 0$), net heating leads to an increase in ρ and thereby an increase in density in the littoral region compared with the pelagic region due to differential heating ($\partial \rho/\partial x < 0$). The same process occurs for a net cooling in the case $T > T_{md}$ ($\alpha > 0$), leading to $\partial \rho/\partial x < 0$ by differential cooling. Reversed lateral density gradients $\partial \rho/\partial x > 0$ are created by differential cooling if $T < T_{md}$ and by differential heating if $T > T_{md}$.

Additional relevant fluid properties include the molecular kinematic viscosity ν and thermal diffusivity κ. Despite being broadly considered constant, both parameters are temperature dependent. The

https://doi.org/10.1017/flo.2024.31 Published online by Cambridge University Press

Table 1. *List of relevant variables and parameters to characterise TS.*

Parameter	Dimensions	Characteristic value	Comment
$\lvert B_0 \rvert$	$m^2\,s^{-3}$	$O(10^{-10})$–$O(10^{-7})$	Surface buoyancy flux (§ 2.3)
$\lvert B_{net,0} \rvert$	$m^2\,s^{-3}$	$O(10^{-10})$–$O(10^{-7})$	Net buoyancy flux (§ 2.3)
$\lvert B_{SW,0} \rvert$	$m^2\,s^{-3}$	0–$O(10^{-7})$	Solar radiative buoyancy flux (§ 2.3)
D	m	$O(10)$–$O(10^2)$	Maximum depth of basin (§ 4.1)
d	m	$O(1)$	Characteristic depth of shallow littoral (§ 4.1)
E	—	$O(10^{-2})$	Net entrainment coefficient (§ 9)
G	—	$O(1)$	Geometrical factor (§ 7.2)
G_{Ro}	—	$O(1)$	Geometrical factor integrating Coriolis (§ 7.2)
g'	$m\,s^{-2}$	$O(10^{-5})$	Reduced gravity (§ 4.1)
$H_{Q,0}$	$W\,m^{-2}$	$[-O(10^2), O(10^2)]$	Surface heat flux (§ 2.3)
$H_{SW,0}$	$W\,m^{-2}$	0–$O(10^3)$	Short-wave radiative flux (§ 2.3)
h_m	m	$O(1)$–$O(10)$	Surface mixed-layer thickness (§ 4.1)
h'_m	m	$O(1)$–$O(10)$	$h'_m = h_m - d$ (§ 4.1)
k_d	m^{-1}	$O(10^{-1})$–$O(1)$	Light attenuation coefficient (Appendix A)
ℓ_{ml}	m	$O(10^2)$–$O(10^3)$	Horizontal length of the littoral zone (§ 4.1)
ℓ_p	m	$O(10)$–$O(10^3)$	Horizontal length of plateau zone (§ 4.1)
ℓ_s	m	$O(10)$–$O(10^3)$	Horizontal length of sloping zone (§ 4.1)
N_s	s^{-1}	$O(10^{-2})$	Buoyancy frequency in surface layer (§ 4.7)
$s, \bar{s}$	—	$O(10^{-3})$–$O(10^{-1})$	Characteristic slope of littoral region (§ 4.1)
T	°C	0–30	Water temperature (§ 2.2)
T_{md}	°C	≈3.98	Temperature of maximum density (§ 2.2)
U	$m\,s^{-1}$	$O(10^{-2})$	Phillips (1966) velocity scale (5.1)
u_t	$m\,s^{-1}$	$O(10^{-2})$	Thermal siphon velocity scale (§ 4.5)
u_*	$m\,s^{-1}$	$O(10^{-3})$–$O(10^{-2})$	Friction velocity (§ 8)
w_c	$m\,s^{-1}$	$O(10^{-3})$	Free convection velocity scale (§ 4.3)
α	$°C^{-1}$	$[-0.68, 3.03] \times 10^{-4}$	Thermal expansion coefficient (§ 2.2)
δ_c	m	$O(10^{-2})$–$O(10^{-1})$	Penetration depth of convective plumes (§ 6.3)
δ_S	m	$O(10^{-1})$–$O(1)$	Thickness of the shear layer (§ 6.3)
δ_ρ	m	$O(10^{-1})$–$O(1)$	Thickness of the density gradient region (§ 6.3)
$\rho(T)$	$kg\,m^{-3}$	995.67–999.95	Equation of state of water (2.2)
$\Delta\rho$	$kg\,m^{-3}$	$O(10^{-3})$	Density difference in lakes (§ 2.2)
τ_{wind}	$N\,m^{-2}$	$O(10^{-3})$–$O(10^{-1})$	Wind shear stress (§ 9)
χ_{MO}	$m\,m^{-1}$		Non-dimensional Monin–Obukhov length (8.1)
τ_B	min	$O(1)$	Onset time scale of thermal convection (§ 4.2)
τ_{RB}	min	$O(10)$–$O(10^2)$	Free convection time scale (§ 4.3)
τ_t	h	$O(1)$–$O(10)$	Transition time scale (§ 4.5)
τ_a	h	$O(1)$	Adjustment time scale (§ 4.6)
τ_{qs}	h	$O(10)$	Quasi-steady time scale (§ 4.6)
τ_{mix}	h	0–$O(10^2)$	Mixing time scale (§ 4.7)
τ_F	h	$O(1)$–$O(10)$	Flushing time scale (§ 5, (5.4))
q_{TS}	$m^2\,s^{-1}$	$O(10^{-3})$–$O(10^{-1})$	TS discharge per unit width (§ 5)

relevant non-dimensional number that encapsulates the information of both molecular parameters is the Prandtl number, $Pr = \nu/\kappa$. In the case of surface water bodies with temperature around 20 °C, $\nu \approx 10^{-6}\,m^2\,s^{-1}$ and $\kappa \approx 1.43 \times 10^{-7}\,m^2\,s^{-1}$, $Pr \approx 7$. However, for freshwater bodies with surface temperatures ranging between 0 °C and 30 °C, Pr varies in the range $5 < Pr < 14$.

https://doi.org/10.1017/flo.2024.31 Published online by Cambridge University Press

2.3. Boundary conditions and external forcing

2.3.1. Forcing mechanisms

This review puts the focus on TS driven by atmospheric heat exchange, including surface heat fluxes at the air–water interface and penetrative solar radiation heat flux (Schmid & Read 2022). We discuss the following five different forcing scenarios.

(i) Steady stabilising forcing: differential heating when surface water temperatures are above T_{md} (§ 3).
(ii) Steady destabilising forcing: differential cooling when surface water temperatures are above T_{md} (§§ 3 and 4).
(iii) Unsteady forcing when surface water temperatures are above T_{md} (§ 6).
(iv) Unsteady forcing by solar radiation when surface water temperatures are below T_{md}, as in ice-covered waterbodies (§ 7.2).
(v) Steady destabilising forcing with a response modulated by wind (§ 8).

2.3.2. Boundary conditions

Conceptual models assume a no-slip bottom boundary and generally ignore any exchange at the sediment–water interface. In the case of the top boundary, we consider the open air–water interface free-to-slip and the ice–water interface of ice-covered waterbodies to be a no-slip surface. In this review, as in most of the literature on TS, we assume no heat flux at the sediment–water interface. Readers interested in the heat exchange at the sediment–water interface (and its impacts) are referred to the works by Hondzo & Stefan (1993), Fang & Stefan (1996), Zdorovennova *et al.* (2021), MacIntyre, Cortés & Sadro (2018), Cortés & MacIntyre (2020) and Perga *et al.* (2023). To resolve the evolution of heat in the aquatic system, we need to characterise the surface heat exchange and the internal heating caused by solar radiation throughout the water column. Details are provided in Appendix A and we only report the main results and final equations below.

The surface heat flux $H_{Q,0}$ (W m^{-2}) results from the combined action of four processes exchanging heat between the atmosphere and the water body: sensible heat exchange, latent heat exchange, incoming and outgoing long-wave radiation (Schmid & Read 2022).

According to the convention in field studies, the heat content of the water body increases if $H_{net,0} < 0$ (net heating) and decreases if $H_{net,0} > 0$ (net cooling). The surface heat flux changes the potential energy of the water column, which is expressed by a surface buoyancy flux per unit mass $B_0 = \alpha g H_{Q,0}/(\rho_0 C_p)$ (W kg^{-1}) (Soloviev & Lukas 2014), where g is the gravitational acceleration (m s^{-2}), C_p is the specific heat of water (J °C^{-1} kg^{-1}) and ρ_0 is a reference density. Surface heat exchange stabilises (stratifies) the water column when $B_0 < 0$ and destabilises it (promoting convection) when $B_0 > 0$. For $T > T_{md}$ ($\alpha > 0$), surface heating stabilises and surface cooling destabilises the water column. The process reverses for $T < T_{md}$ and $\alpha < 0$. Considering the same approximation made in (A4), the net buoyancy flux is

$$B_{net,0} = B_0 + B_{SW,0} = \frac{g\alpha}{\rho_0 C_p} H_{Q,0} + \frac{g\alpha}{\rho_0 C_p} H_{SW,0}, \tag{2.3}$$

where $H_{SW,0}$ is the solar radiation reaching the air–water interface and $B_{SW,0}$ is the solar radiative buoyancy flux at the surface.

3. Steady forcing with stabilising or destabilising effects

In this section we discuss the effect of a steady surface forcing with stabilising or destabilising effects only for aquatic systems with temperatures $T > T_{md}$; see figure 2. Although the stabilising and destabilising cases share common principles, they should not be treated as symmetrical cases.

https://doi.org/10.1017/flo.2024.31 Published online by Cambridge University Press

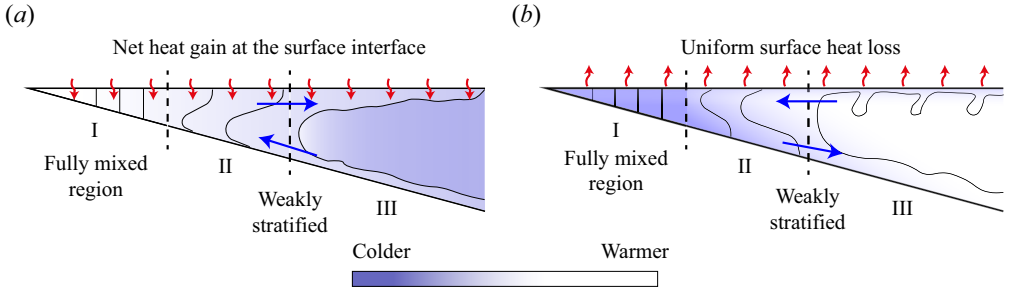

Figure 4. *Schematic of isotherm distributions for different convective flow sub-regions in nearshore waters with $T > T_{md}$ due to (a) differential heating and (b) differential cooling. Adapted from Mao, Lei & Patterson (2009, 2010). Note that Mao et al. (2009) reported rising thermal plumes at the bottom of the region (III). These instabilities can be attributed to the model's bottom boundary condition, where reflected heat leads to localised excess heating.*

3.1. Steady differential heating above T_{md} (stabilising forcing)

Differential heating above T_{md} corresponds to the case of stabilising surface buoyancy flux over a sloping boundary. A series of numerical investigations explored the influence of uniform surface heating and internal heating on freshwater bodies with varying depths, employing a basic geometry to model the littoral environment – a triangular domain connected to a flat interior basin, as shown in figure 3(*a*) (Lei & Patterson 2002, 2003; Mao *et al.* 2009; Mao, Lei & Patterson 2012; Yu, Patterson & Lei 2015). The equation of state for water was taken as a linear function between temperature and density, with temperatures above T_{md}. These numerical experiments consistently showed the emergence of TS propelled by differential heating. In this scenario, shallow waters, warming more rapidly than their deeper counterparts, become less dense, initiating a two-layer exchange flow, directing upslope deep waters toward the littoral and offshore shallow waters across the surface, as illustrated in figure 4(*a*). Thermal siphons exhibit three distinct regimes across the sloping region. From the very shallow to deeper waters, the system shows a 'conductive' region I with vertical isotherms, a 'stable convective' region II characterised by a two-layer exchange flow, and an 'unstable convective' region III where a surface flow coexists with a bottom convective layer. The spatial boundaries of these regions and regimes were determined by the slope of the wedge-like basin and the global Rayleigh number of the system (Mao *et al.* 2009). As mentioned in the introduction, this case is rarely observed in the field and is not further developed in this review. It is however important to remind the reader that the dynamics induced by stabilising surface buoyancy flux over a sloping boundary are not analogous to those induced by a destabilising surface buoyancy flux. For instance, the downslope flow resulting from the destabilising forcing is affected by the development of a convective mixed layer (see § 6.3) that is obviously not present in the stabilising forcing case.

3.2. Steady differential cooling above T_{md} (destabilising forcing)

Differential cooling above T_{md} corresponds to the case of destabilising surface buoyancy flux over a sloping boundary. In a wedge-shaped water basin with a uniform slope, Horsch & Stefan (1988) and Horsch, Stefan & Gavali (1994) conducted pioneering experimental and numerical investigations, unravelling the physical processes behind the formation of TS by differential cooling (see schematic in figure 4*b*). As thermal plumes sinking from the surface interact with the sloping bottom, they contribute to the creation of a downslope gravity current in the shallowest region. By mass conservation, this thermally induced gravity current is compensated by a surface current toward the shore, thus establishing an overturning circulation characterised by a two-layer exchange flow: the bottom layer transports colder, denser waters downslope (offshore) and the surface layer conveys warmer, lighter waters towards the

https://doi.org/10.1017/flo.2024.31 Published online by Cambridge University Press

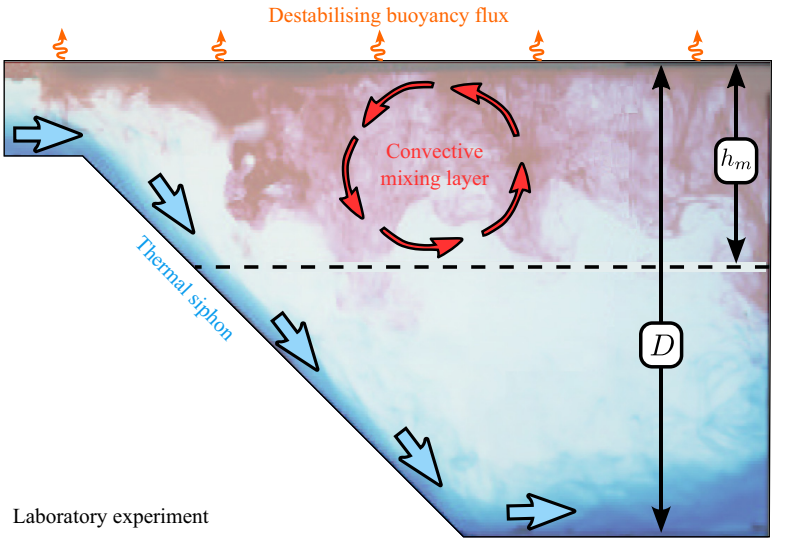

Figure 5. *Photograph showing the circulation of dye in a laboratory experiment. The red dye is placed into the convective mixing layer and the blue dye is placed into the gravity current. Adapted from Wells (2001).*

shore. Numerical studies exploring the consequences of surface cooling in wedge-like domains identified three regimes across the sloping region, as in the case of differential heating (Lei & Patterson 2005; Mao *et al.* 2010; Papaioannou & Prinos 2023).

Wells & Sherman (2001) explored TS via laboratory experiments using a distinct basin design, akin to the schematic in figure 3(*c*). The basin comprised a flat shelf connected to a deeper area via a sloping bottom. Before the TS formation, the authors noted an active phase of vertical mixing, resulting in a significant horizontal temperature difference between shallow and deep regions. They visualised the circulation using dye, as shown in figure 5, and noticed that the dye injected in the surface region was transported downward into the convective mixing layer by thermal plumes, while the dye injected on the shallow plateau was transported as a density current ultimately filling in the deep water. To estimate gravity current initiation, Wells & Sherman (2001) utilised the 'transition time scale' from Finnigan & Ivey (1999), initially derived for buoyancy-driven exchange between basins separated by a sill with a localised destabilising surface buoyancy flux. A fundamental result by Wells & Sherman (2001) was that a system can reach a quasi-steady state if the area of the shallow basin is equal to the area of the deep basin. As we discuss later, the theoretical and experimental study by Finnigan & Ivey (1999) on the buoyancy-driven interbasin exchange flow over a sill remains pivotal for understanding the transient dynamics of a TS. The latter authors identified three dynamic regimes in the exchange flow across the sill: localised convection, progressive growth of density difference and the development of a transient exchange flow until a quasi-steady state. The characterisation of the regime linked to horizontal convection, observed by Finnigan & Ivey (1999), relied on an inertia–buoyancy balance, similar to the analysis by Phillips (1966) describing convective circulation in the Red Sea.

Utilising laboratory and numerical experiments, Bednarz, Lei & Patterson (2008*a*, 2009*a*) studied the onset of natural convection and the subsequent horizontal convective flow resulting from a destabilising surface heat flux on an initially isothermal water body of uniform slope connected to a flat interior basin. Although the authors focused on characterising the early convective stage theoretically, their experiments showed the existence of spatially varying convective regimes that motivated further numerical studies, including the work by Mao *et al.* (2010).

https://doi.org/10.1017/flo.2024.31 Published online by Cambridge University Press

4. Formation of cooling-driven TS

4.1. Conceptual model for TS in stratified water bodies

Ulloa *et al.* (2022) proposed a two-dimensional (2-D) conceptual model to investigate the development of TS driven by surface cooling in water bodies of varying depth with temperatures $T \geq T_{md}$. The model integrates canonical topographic features observed in natural aquatic systems: an almost flat shallow plateau (or shelf) of length ℓ_p, joined through a sloping (S) bottom region to the interior (I) stratified basin, which has a surface layer h_m, as shown in figure 3(*c*). The characteristic scales of the plateau are its horizontal length ℓ_p and its depth d. The depth-dependent sloping zone has a horizontal length ℓ_s and a characteristic slope $\bar{s} = (h_m - d)/\ell_s = h'_m/\ell_s$. The sloping bottom zone extends until the point where the base of the surface mixed layer intersects the bottom boundary. In the case studied here, the maximum depth of the water body D is much smaller than the horizontal length scale $\mathcal{L}$ of the system, i.e. $D/\mathcal{L} \ll 1$, which allows treating these system environments as 'shallow waters'.

The conceptual model in figure 3(*d*) considers an initial water temperature distribution defined by a stable and smooth two-layer stratification, i.e.

$$T(x, z, t = 0) = T_b + \frac{\Delta T}{2}\left\{1 + \tanh\left(\frac{z - z_m}{\delta_m}\right)\right\}, \tag{4.1}$$

with T_b and $T_s = T_b + \Delta T$ representing the bottom layer temperature and surface layer temperature, respectively. The transition between the bottom layer and the surface layer occurs over a length scale δ_m and the position of the maximum temperature gradient, or thermocline, is initially at z_m. Both layers may exhibit weak temperature gradients or weak thermal stratification before a phase of destabilising surface cooling starts. The model (4.1) for the background temperature distribution represents well various thermally stratified lake systems featuring distinct epilimnion, metalimnion and hypolimnion regions. From the equation of state of water (2.1) and (4.1), we can determine the background density structure and the density difference between the top layer and bottom layer, $\Delta\rho$, resulting from the temperature difference between layers ΔT. This density difference sets the actual reduced gravity that fluid parcels experience within the stratified body, $g' = (\Delta\rho/\rho_0)g$.

Considering the conceptual model in figure 3(*c*), Ulloa *et al.* (2022) inferred the existence of various convective regimes and phases of the development of TS. In this section we revisit the derivation of the theoretical time scales associated with the emergence of such convective regimes, starting from the time taken for thermal instabilities to grow from the air–water interface to the development of a cross-shore overturning circulation between the shallow and deep interior waters. The time scales involved in the lifespan of TS and discussed in this review are summarised in figure 6. Some of these time scales can only be determined from high-fidelity numerical experiments or highly controlled laboratory experiments, such as the time scale associated with the onset of thermal instabilities (Bednarz, Lei & Patterson 2008*b*, 2009*b*). In contrast, other time scales can be readily estimated from parameters directly measured in field experiments and comprehensive numerical studies. These time scales enable the interpretation of the different convective dynamics involved in the development of TS, as shown by Doda *et al.* (2022) and Ramón *et al.* (2022).

4.2. Onset of thermal instabilities – τ_B

We start by discussing the emergence of thermal instabilities that will originate primal motions. Let us assume that the fluid is initially at rest, with a uniform temperature near the surface. The air–water interface is subject to a 'surface cooling' rate H_0. In this scenario, water molecules at the surface interface cool faster than those beneath the surface. Prior to the onset of thermal instabilities, the time-dependent

https://doi.org/10.1017/flo.2024.31 Published online by Cambridge University Press

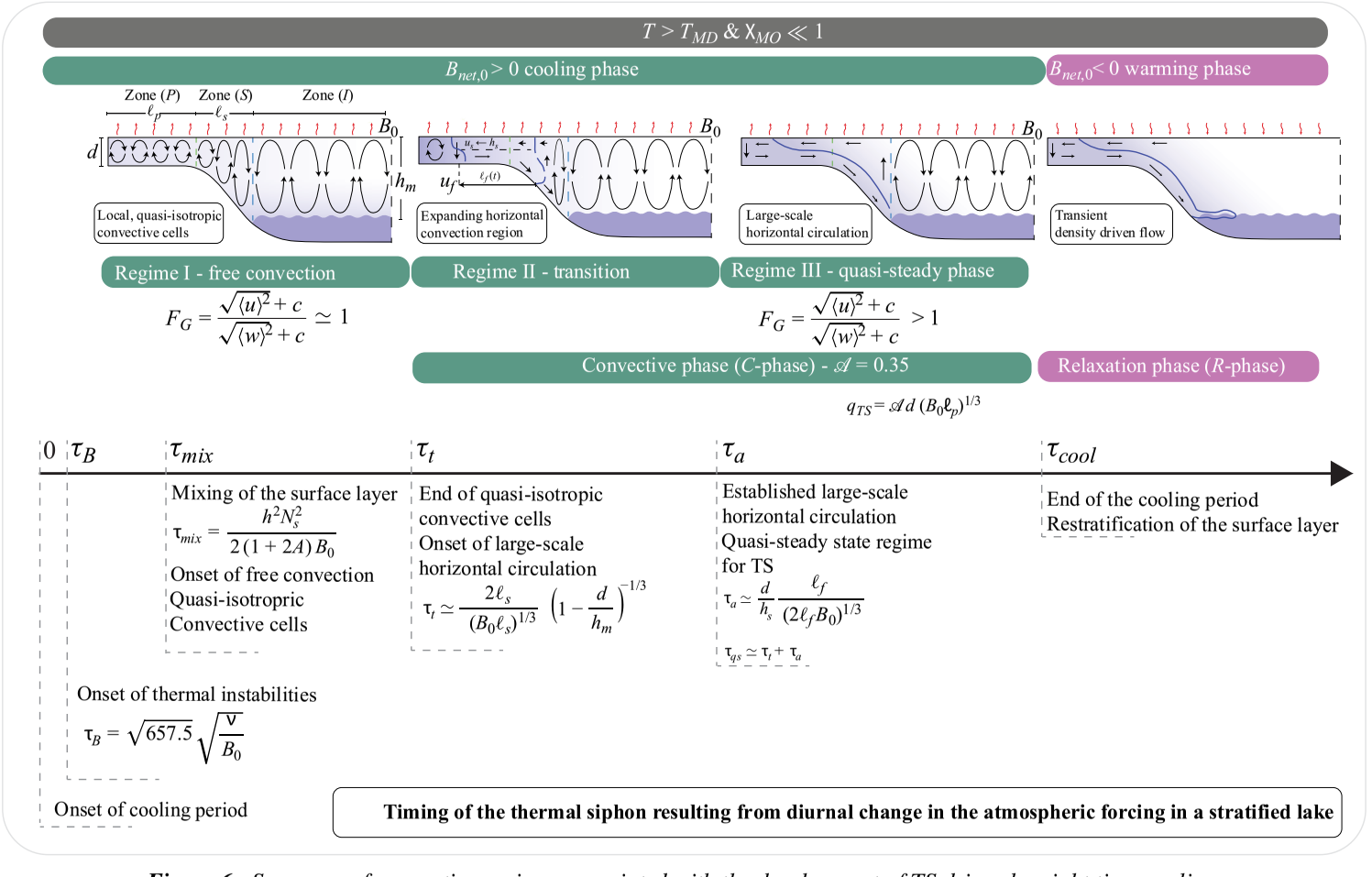

Figure 6. *Summary of convective regimes associated with the development of TS driven by night time cooling.*

temperature drop at the surface is determined by the following expression (Bednarz *et al.* 2009*a*):

$$\Delta T(t) = -2\frac{H_0}{K}\sqrt{\frac{t}{\kappa\pi}}. \tag{4.2}$$

Here K is the water thermal conductivity. Such a temperature drop occurs over the conductive thermal boundary layer beneath the surface, which scales as $\delta_T \sim \sqrt{\kappa t/\pi}$. The onset time scale of the instabilities can be estimated considering the critical Rayleigh number for free-slip boundaries, $Ra_c \approx 657.5$. Utilising expression (4.2), we can determine a time-dependent local Rayleigh number

$$Ra_L(t) \equiv \frac{g\alpha\Delta T(t)\delta_T^3(t)}{\nu\kappa} = 2g\alpha\frac{H_0}{K\nu\kappa^2}\left(\frac{\kappa t}{\pi}\right)^2 \tag{4.3}$$

and evaluate the time needed for (4.3) to overcome the critical Rayleigh number. From this analysis, it yields a time scale for the onset of thermal instabilities (Bednarz *et al.* 2009*a*):

$$\tau_B \simeq \frac{Ra_c}{Ra_L} = \sqrt{657.5}\sqrt{\frac{\nu}{B_0}}. \tag{4.4}$$

For $B_0 \sim 10^{-10}$–$10^{-8}\,\mathrm{W\,kg^{-1}}$, τ_B may vary from minutes to tens of minutes.

4.3. Characteristic time scale of free convection – τ_{RB}

Upon the initiation of convection, the sinking speed of thermal plumes can be estimated using an energy scaling relationship between kinetic energy transport and buoyancy flux, known as the Deardorff convective velocity scale $w_c \simeq (B_0 h_m)^{1/3}$ (Deardorff 1970). The magnitude of w_c is of the order of $10^{-3}\,\mathrm{m\,s^{-1}}$, and h_m represents the convective (vertical) length scale and is in the range of $O(1$–$10)$ m. These scales allow us to derive a characteristic time scale for free convection, analogous to Rayleigh–Bénard-type convection:

$$\tau_{RB} \simeq \frac{h_m}{(B_0 h_m)^{1/3}}. \tag{4.5}$$

This represents the time needed for the initial convective plumes to interact with either the sediment–water interface or the thermocline. In simpler terms, the time scale τ_{RB} characterises the lifespan of the very early free convective regime, where the system remains unaffected by the presence of the bottom boundary.

The early stage of free convection is brief, and this review does not delve deeply into this initial convective phase. Interested readers are referred to Bednarz *et al.* (2008*a*, 2009*a*) for more details. Here, our emphasis is on understanding the convective processes that unfold after thermals engage with the lower physical boundaries, leading to the development of a large-scale overturning circulation across the sloping region – the TS.

4.4. Transition towards a quasi-steady convective regime

Figure 6 illustrates three distinct convective stages followed by a baroclinic adjustment (see § 5). In the initial phase, fluid motion is dominated by local quasi-isotropic convective cells across the various zones, as shown in figure 6 (regime I). Rayleigh–Bénard-type convection facilitates the local vertical mixing of temperature in the surface layer. Simultaneously, a cross-shore temperature gradient develops due to differential cooling between shallow and deep waters (e.g. volume difference), leading to the gradual horizontal expansion of convective cells. This initial phase occurs within the time window $\tau_{RB} < t \lesssim \tau_t$.

Following the 'transition time scale', τ_t, the fluid motion becomes progressively dominated by a horizontal density gradient. This sets the stage for initiating a large-scale overturning circulation from

https://doi.org/10.1017/flo.2024.31 Published online by Cambridge University Press

zone (S), which holds the most significant cross-shore density gradient. This second phase is termed regime II. Figure 6 illustrates the expansion of the horizontal convective cell toward the shallowest lateral boundary due to baroclinic adjustment. The lateral growth happens at a rate $u_f \equiv \mathrm{d}\ell_f/\mathrm{d}t$, with ℓ_f denoting the position of the shore-directed front from where the horizontal convection region originates. The large-scale overturning circulation takes the form of a two-layer exchange flow, with a surface layer h_s moving toward the lateral boundary and the bottom layer flowing into the interior. Regime II unfolds over a time scale τ_a, representing the time required by the large-scale overturning circulation to reach the (shallowest) lateral boundary, as depicted in figure 6. After a time scale $\tau_{qs} \simeq \tau_t + \tau_a$, we anticipate the large-scale overturning circulation to attain a quasi-steady state, referred to as regime III.

Next, we derive the dynamic regimes and associated time scales that govern the transition from one regime to the subsequent one. For conciseness, mathematical details are reported in Appendices A–D.

The evolution of the depth-averaged temperatures in the three zones (P), (S) and (I), as illustrated in figure 6, can be approximated through a simplification of the heat balance during the free convection regime (e.g. regime I). The details of the calculation are provided in Appendix B. We denote the vertical average of a function $\varphi(t, z)$ over a layer h as $\langle\varphi\rangle_{(\cdot)} = h^{-1}\int_h \varphi(t, z)\,\mathrm{d}z$. Here, the subscript $(\cdot)$ represents whether it pertains to zone (P), (S) or (I).

Starting from the initial time $t_0 = 0$, the average temperature within zone (P) changes as follows:

$$\langle T\rangle_{(P)} = \langle T(t_0)\rangle_{(P)} - \frac{I_0}{d}t. \tag{4.6}$$

Here $I_0\,(= H_0/(\rho_0 C_p))$ is the kinematic heat flux. In zone (I) the average temperature can be approximated as

$$\langle T\rangle_{(I)} \approx \langle T(t_0)\rangle_{(I)} - \frac{I_0}{h_m}t. \tag{4.7}$$

In the sloping region (S), the x-dependent depth-averaged temperature evolution, $\langle T\rangle_{(S)}$, follows a similar pattern to (4.6) and (4.7) but is normalised by the local depth, $D_B(x)$.

Given our assumption that $T > T_{md}$ and the small temperature drops during the cooling phase throughout the day relative to T_s (approximately $0.1^\circ\mathrm{day}^{-1}$), we can rely on a local linearization of the equation of state (2.1) to accurately estimate the density, ρ, and buoyancy, b, for each zone:

$$\frac{\langle\rho\rangle_{(\cdot)}}{\rho_0} - 1 = \alpha(\langle T\rangle_{(\cdot)} - T_0) \quad \text{and} \quad \langle b\rangle_{(\cdot)} = -g\left(\frac{\langle\rho\rangle_{(\cdot)}}{\rho_0} - 1\right) = -g\alpha(\langle T\rangle_{(\cdot)} - T_0). \tag{4.8a,b}$$

The time-dependent, cross-shore pressure gradient between zones (P) and (I) can be estimated as (see Appendix D)

$$\frac{1}{\rho_0}\frac{\partial p}{\partial x}\bigg|_{z=D-d} \approx \frac{dg\alpha}{\ell_s}(\langle T\rangle_{(I)} - \langle T\rangle_{(P)}) = -\frac{B_0}{\ell_s}\left(1 - \frac{d}{h_m}\right)t. \tag{4.9}$$

In general, the horizontal temperature difference, $\langle T\rangle_{(I)} - \langle T\rangle_{(P)}$, is substantially smaller than the temperature difference between the top and bottom layers in the stratified interior region (I), ΔT_z.

4.5. Transition time scale – τ_t

We aim at determining the time scale at which the cross-shore pressure gradient balances the inertial terms in (D2), i.e.

$$-\frac{\partial}{\partial x}\left(\frac{p}{\rho_0}\right) \simeq \frac{\partial u}{\partial t} \simeq \frac{\partial}{\partial x}\left(\frac{u^2}{2}\right). \tag{4.10}$$

https://doi.org/10.1017/flo.2024.31 Published online by Cambridge University Press

From (4.10) and the cross-shore pressure gradient in (4.9), we derive two horizontal velocity scales:

$$\frac{\partial u}{\partial t} \simeq -\frac{\partial}{\partial x}\left(\frac{p}{\rho_0}\right) \quad \rightarrow \quad u \simeq \frac{B_0}{\ell_s}\left(1-\frac{d}{h_m}\right)\frac{t^2}{2}, \tag{4.11}$$

$$\frac{\partial}{\partial x}\left(\frac{u^2}{2}\right) \simeq -\frac{\partial}{\partial x}\left(\frac{p}{\rho_0}\right) \quad \rightarrow \quad u \simeq \sqrt{2B_0\left(1-\frac{d}{h_m}\right)}\,t. \tag{4.12}$$

The three-way balance (4.10) is achieved at a time scale τ_t at which the velocity scale u allows balancing the inertial terms with the cross-shore pressure gradient. Therefore, equating expressions (4.11) and (4.12) yields

$$\tau_t \simeq \frac{2\ell_s}{(B_0\ell_s)^{1/3}}\left(1-\frac{d}{h_m}\right)^{-1/3}. \tag{4.13}$$

The time scale τ_t defines the transition from regime I to regime II, schematised in figure 6, and at τ_t, the characteristic horizontal velocity scale, u_t, is given by

$$u_t \simeq 2(B_0\ell_s)^{1/3}\left(1-\frac{d}{h_m}\right)^{1/3}. \tag{4.14}$$

The exchange flow associated with the large-scale overturning circulation is expected to develop in the zone with the maximum cross-shore pressure gradient, i.e. zone (S). Considering that this zone has a uniform slope, we expect the large-scale overturning circulation to emerge at about the middle of zone (S), as shown later via numerical experiments.

4.6. Adjustment and quasi-steady time scales – τ_a, τ_{qs}

We now aim to determine the time scale required by the large-scale overturning circulation to reach the lateral boundary in zone (P) and be adjusted to a new equilibrium state. This adjustment time scale, τ_a, depends on the horizontal length of the nearshore area between the point from where the TS starts and the lateral boundary. During regime II, this nearshore area can be split into two regions: a region of length $\ell_f(t)$ (measured from the starting point) that grows in time due to the lateral expansion of the large-scale overturning circulation, and its neighbouring region that shrinks in time, where quasi-isotropic convective cells dominate the local flow, as depicted in figure 6. In this shrinking well-mixed zone, denoted as (LP), the average buoyancy results from the expressions (B3) and (4.8*a*,*b*),

$$\langle b\rangle_{(LP)} = -\frac{B_0}{d}t. \tag{4.15}$$

In zone (LP) the temperature and buoyancy are continuously decreasing, and $\langle b\rangle_{(LP)}$ matches the buoyancy at the left front of the horizontal convective cell, $\ell_f(t)$. Following the arguments by Phillips (1966), we assume that the momentum of the surface layer current u_s and buoyancy are found in an inertia–buoyancy balance. This assumption implies that the flow within the horizontal convective cell scales as

$$u_s \simeq (2\langle b\rangle_{(LP)}h_s)^{1/2}, \tag{4.16}$$

where h_s is the thickness of the surface exchange layer, shown in figure 6. Additionally, we may also consider that the surface buoyancy flux, B_0, across ℓ_f is balanced with the production of kinetic energy, which leads to the scaling velocity $u_s \simeq (2B_0\ell_f)^{1/3}$. Hence, the above two velocity scales are equal when

$$\langle b\rangle_{(LP)} \simeq \frac{(2B_0\ell_f)^{2/3}}{2h_s}. \tag{4.17}$$

https://doi.org/10.1017/flo.2024.31 Published online by Cambridge University Press

By equating (4.15) and (4.17), we can derive the time scale required by the exchange flow to reach the lateral boundary. The latter is reached when $\ell_f(\tau_a) \simeq \ell_p + \ell_s/2$,

$$\tau_a \simeq \frac{d}{h_s}\frac{\ell_f}{(2\ell_f B_0)^{1/3}}, \tag{4.18}$$

where τ_a represents the time scale needed for the large-scale overturning circulation to fully adjust across zones (P) and (S). As a consequence, the time scale $\tau_{qs} \simeq \tau_t + \tau_a$ represents the time required to achieve the quasi-steady state that characterises regime III.

4.7. What if the surface layer is thermally stratified?

The surface layer, schematised in figure 3(*c*), may have an initial temperature gradient, particularly in the vicinity of the very surface, characterised by a buoyancy frequency N_s (e.g. Imberger 1985). In this situation, the destabilising surface cooling will erode and mix the surface layer until it encounters a physical barrier. This barrier could be either the sediment–water interface in the littoral region or the seasonal thermocline zone in the interior or pelagic zone. We can estimate the time required to mix the surface layer by using the evolution equation for a convective mixing layer (Zilitinkevic 1991) given as follows:

$$\frac{\mathrm{d}h}{\mathrm{d}t} = (1 + 2A)\frac{B_0}{hN_s^2}. \tag{4.19}$$

Here, the coefficient $A \approx 0.2$ is an empirical parameter. For a detailed derivation of (4.19) and more information about A, readers are referred to Zilitinkevic (1991). It is important to note that the evolution equation (4.19) accounts explicitly for the expansion of the convective mixing layer of depth h due to a destabilising surface buoyancy flux B_0.

Given that the lakes' surface layers exhibit weak stratification due to daytime solar radiation absorption in the epilimnion, the density's vertical distribution tends to be approximately linear. Consequently, the buoyancy frequency N_s is almost constant and significantly weaker than the buoyancy frequency associated with the seasonal thermocline, as illustrated in figure 3(*c*). Assuming N_s to be 'uniform' through the surface layer, the evolution equation for the surface convective mixing layer (4.19) yields an analytical solution:

$$h(t) = \sqrt{h_0^2 + 2(1 + 2A)\frac{B_0}{N_s^2}(t - t_0)}. \tag{4.20}$$

Here, h_0 represents the initial thickness of the convective mixing layer at the initial time t_0. If both initial conditions are taken as 'zero', a straightforward expression for the time taken to mix the surface layer is obtained. This time, denoted as the initial mixing time scale by Doda *et al.* (2022), is given by

$$\tau_{mix} = \frac{h^2 N_s^2}{2(1 + 2A)B_0}. \tag{4.21}$$

We should note that the time required to mix shallow waters may differ from the time needed to mix the surface layer within the interior stratified zone. If $\tau_{mix} > 0$, time scales linked to the various convective regimes experience a temporal shift. In particular, the time scale for the 'onset' or development of a TS due to differential cooling is more accurately predicted by '$\tau_{mix} + \tau_t$', as shown by Doda *et al.* (2022).

4.8. Numerical and field experiments

The theoretical time scales predicting the different stages at which a TS develops can be tested with numerical and field experiments (Doda *et al.* 2022; Ramón *et al.* 2022; Ulloa *et al.* 2022). Ulloa *et al.*

https://doi.org/10.1017/flo.2024.31 Published online by Cambridge University Press

(2022) confirmed the theoretical transition time scale τ_t and quasi-steady time scale τ_{qs} through 2-D high-fidelity spectral numerical experiments at high Rayleigh numbers, covering a range of nearshore slopes observed in aquatic systems, $1\,\% < \bar{s} < 10\,\%$. In their assessment, the authors introduced the flow geometry parameter, F_G, denoted as

$$F_G \equiv \frac{\sqrt{\langle u^2 \rangle} + c}{\sqrt{\langle w^2 \rangle} + c}, \tag{4.22}$$

where $\langle u \rangle$ and $\langle w \rangle$ represent the space-averaged horizontal and vertical velocity components over zone (P), defined as the plateau nearshore region, figure 6, respectively. The constant $c \ll \sqrt{\langle u \rangle^2}, \sqrt{\langle w \rangle^2}$ is a regularisation term preventing a singularity when fluid is at rest before the onset of thermal instabilities around τ_B. Figure 7 shows the time series of F_G for different nearshore topographic conditions, highlighting that F_G captures the three convective regimes associated with TS development. During regime I, $t/\tau_t < 1$, F_G hovers around 1, representing a quasi-isotropic flow geometry where the magnitudes of horizontal and vertical velocity components are statistically similar – as shown in figure 7(*a*). In regime II, $t/\tau_t \geq 1$, F_G accurately represents the progressive growth of an overturning circulation that starts in zone (S) but that propagates in time through zone (P) (figure 6). Here, the velocity field evolves into a more elliptical geometry, becoming predominantly horizontal, causing F_G to boldly exceed 1. To identify regime III, figure 7(*b*) shows that F_G reaches a plateau for $t/\tau_{qs} \geq 1$, indicating the theoretically expected quasi-steady phase of regime III. The final value is in the range $1 < F_G < 10$ for a wide range of forcing and bathymetry, yet, there is no study that systematically investigates a possible parameterisation for the plausible values of F_G can attain at quasi-steady state. Before this phase, i.e. $t/\tau_{qs} < 1$, F_G exhibits the transient phase associated with regimes I and II. Similar parameterisation of the quasi-steady time scale can be obtained from three-dimensional (3-D) numerical experiments using a hydrostatic Reynolds-averaged Navier–Stokes (RANS) model (Ramón *et al.* 2022).

Field experiments carried out at Lake Rotsee, Switzerland, by Doda *et al.* (2022) explored the validity of the conceptual model presented in § 4 and figure 6 in a real-scale system. These experiments accurately determined the development of TS in the littoral region of natural aquatic environments by the theoretical transition time scale, τ_t. *In-situ* observations shown in figure 8 showcase two days characterised by almost uniform night-time surface cooling, resulting in a consistent destabilising surface buoyancy flux B_0 that triggered TS after an initiation period of duration $\tau_{mix} + \tau_t$. Using the time scales presented in § 4, it is also possible to infer the seasonality of TS in a specific lake. Thermal siphons would form on a given day if the cooling period when $B_0 > 0$ lasts longer than the initiation period $\tau_{mix} + \tau_t$. For the case of Lake Rotsee (Doda *et al.* 2022), the mixing time scale $\tau_{mix} > O(10)$ h was too long in early summer (e.g. N_s^2 is too strong) and TS could barely develop despite the high B_0. The optimal period for TS formation was observed in fall with still elevated B_0 but reduced N_s^2, which decreased $\tau_{mix} < O(1)$ h. In winter, B_0 was strongly reduced and τ_t increased from $O(1)$ h in summer to $O(10)$ h, which limited the development of TS. Overall, the theoretical model outlined in § 4 precisely captures the fluid dynamics observed in lakes (Ulloa *et al.* 2022).

5. Transport scaling

The cross-shore transport induced by a destabilising buoyancy flux at the water surface can be estimated from measurable physical quantities using scaling formulae derived from theoretical and laboratory studies. Based on the pioneer study by Phillips (1966), the horizontal velocity scale of a TS is

$$U = c_u (B_0 \ell_l)^{1/3}, \tag{5.1}$$

where ℓ_l is the horizontal length scale of the littoral shallow water region, as proposed by Wells & Sherman (2001), and c_u is a proportionality coefficient. The velocity scaling (5.1) arises directly from

https://doi.org/10.1017/flo.2024.31 Published online by Cambridge University Press

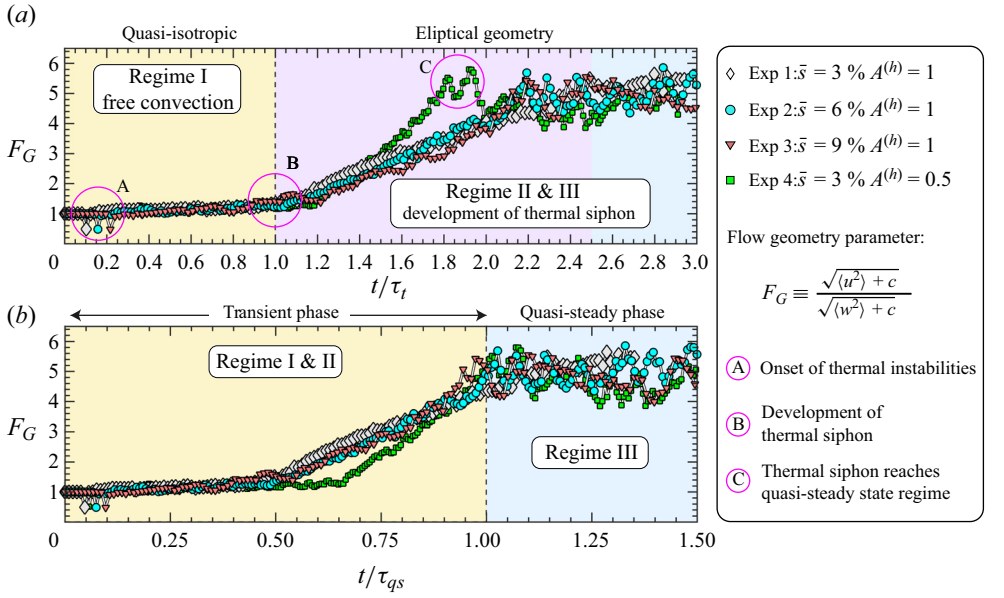

Figure 7. *Different time scales associated with the TS development, extracted from numerical experiments. Panel (a) shows the flow geometry, F_G, as a function of the non-dimensional time t/τ_t. Circle A denotes the onset of thermal instabilities; circle B highlights the time for the transition to horizontal circulation (i.e. TS development). Panel (b) illustrates F_G as a function of the non-dimensional time t/τ_{qs}. All simulations hold $Pr = 7$, and the destabilising thermal forcing, quantified by the Rayleigh number in (E1a–c), is $Ra = 10^5$. Shaded areas correspond to the different convective regimes described in figure 6. Here $A^{(h)}$ is the ratio between the horizontal length scale of the plateau and the slope regions. Adapted from Ulloa et al. (2022).*

the energy balance between the destabilising surface buoyancy flux B_0 and the kinetic energy transport across a characteristic length scale ℓ. Although the classic velocity scale $U \sim \sqrt{g(\Delta\rho/\rho_0)\ell}$ linked to density currents forced by a thermally controlled cross-shore pressure gradient (see Phillips 1966) can be derived by considering the horizontal density anomaly generated by the surface buoyancy flux and assuming that momentum is gravity driven, we deliberately avoid adopting this scale. The rationale is rooted in the scale's dependence on the dynamic variable $\Delta\rho$, which proves challenging to estimate *a priori*, especially in the context of TS.

The unit-width discharge is defined from (5.1) as (Phillips 1966)

$$q_{TS} = c_q (B_0 \ell_l)^{1/3} d_l, \tag{5.2}$$

where $d_l = V_l/\ell_l$ (V_l per unit width) is the characteristic depth of the littoral (l standing for littoral) and c_q is a proportionality coefficient. Sturman *et al.* (1999) and Wells & Sherman (2001) provided a similar slope-dependent discharge scale based on laboratory experiments in a basin with constant slope bathymetry, $\bar{s}$, with a characteristics length scale ℓ_s connected to a uniform-depth basin, as schematised in figure 3(*a*). In a steady-state scenario and for small slopes, Sturman *et al.* (1999) demonstrated, using scaling arguments, that the cross-shore exchange flow is proportional to $q \sim B_0^{1/3}(\ell_s \bar{s})^{4/3}$, and determined the empirical expression

$$q_S = 0.24(B_0 \ell_s)^{1/3} \ell_s \left(\frac{\bar{s}}{1+\bar{s}}\right)^{4/3}. \tag{5.3}$$

https://doi.org/10.1017/flo.2024.31 Published online by Cambridge University Press

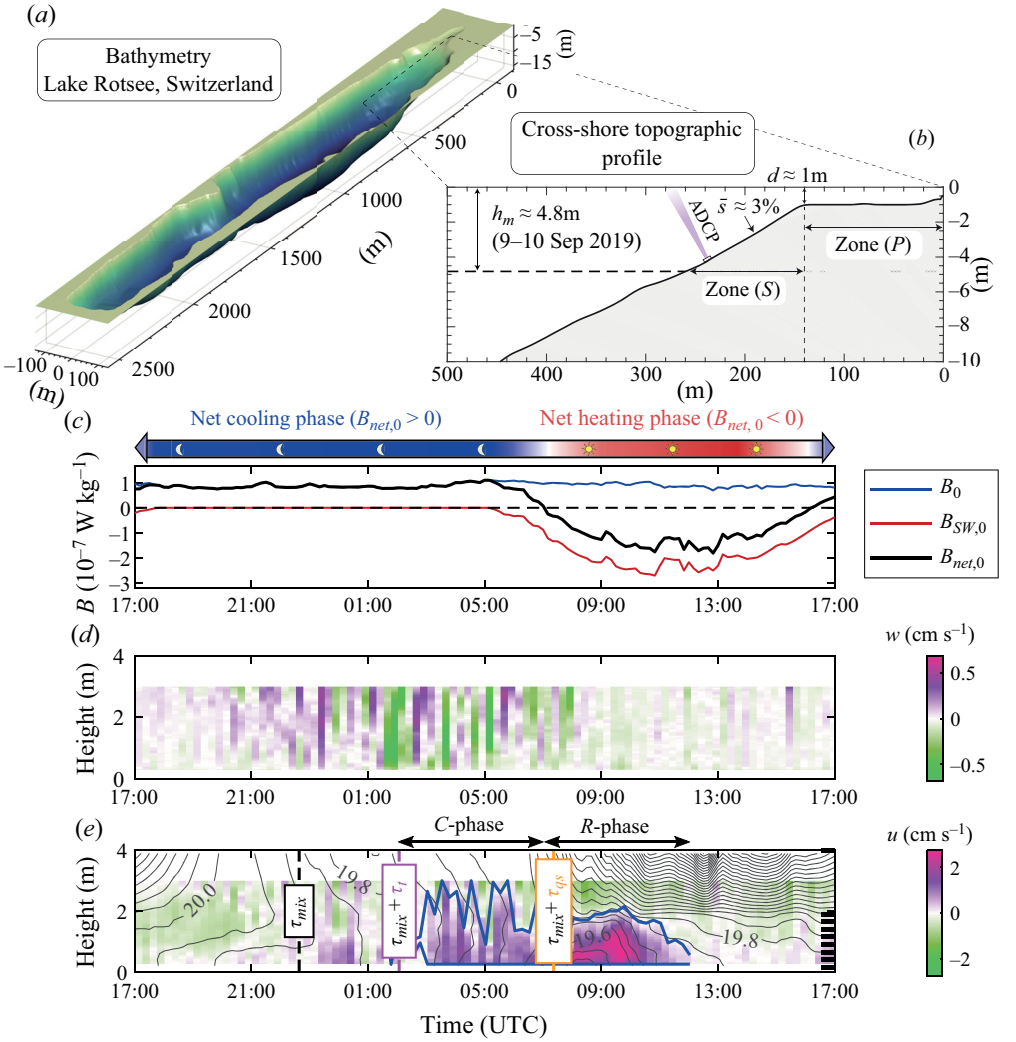

Figure 8. *Panel (a) illustrates Lake Rotsee bathymetry. Panel (b) shows the cross-shore topographic profile of the northeast side basin, highlighting the average depth of zone (P), $d \approx 1$ m, the average slope $\bar{s} \approx 3$ % of zone (S) and the depth of the surface mixed layer $h_m \approx 4.8$ m. (c) Time series of surface buoyancy fluxes defining the cooling and heating phases on 9–10 September 2019. (d) Vertical velocity profile. Positive (purple) values correspond to a flow moving upward. Strong vertical movements are the signature of convective plumes. (e) Cross-shore velocity profile. Positive (purple) values correspond to a flow moving offshore (southwestward flow, highlighted by the blue line). In (d,e) 'Height' refers to the distance from the bottom at the observation location. Black lines are 0.05 °C isotherms linearly interpolated from a thermistor chain (vertical resolution indicated with the horizontal ticks on the right axis). The theoretical time scales τ_{mix}, τ_t and τ_{qs} are indicated. They define the duration between the start of the cooling phase and (i) the end of the vertical mixing period (τ_{mix}), (ii) the end of the initiation period ($\tau_t + \tau_{mix}$) and (iii) the quasi-steady-state regime ($\tau_t + \tau_{qs}$). Two dynamic phases, defined as the convective (C) and relaxation (R) phases, are identified after the TS formation (see § 6.3). Adapted from Ulloa et al. (2022) and Doda et al. (2022).*

It is noteworthy that ℓ_s is shorter than ℓ_{ml}. While this discrepancy is insignificant for small lakes or shallow thermoclines, defining the horizontal length scale becomes crucial and requires careful consideration when investigating the impact of differential cooling on deep mixing in large lakes. Indeed,

https://doi.org/10.1017/flo.2024.31 Published online by Cambridge University Press

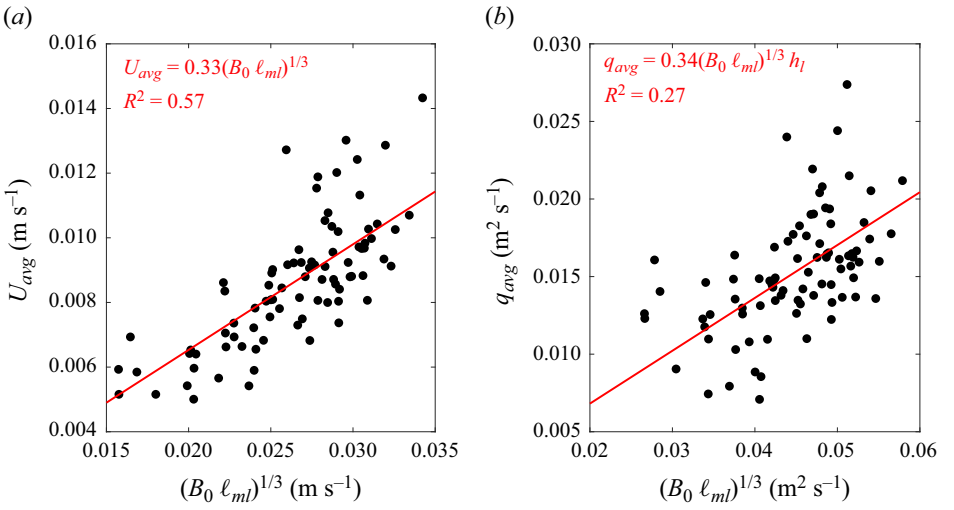

Figure 9. *(a) Daily averaged cross-shore velocity, (b) daily averaged unit-width discharge. The equation of the linear regressions with 0 intercept and the coefficient of determination (R^2) are shown. Adapted from Doda et al. (2022).*

for natural aquatic systems, characterised by complex littoral topographies, it remains challenging to define accurately the relevant horizontal length scale. The definition of the littoral zone is prone to different interpretations. In the following, we refer to the horizontal length scale as the cross-shore distance at which the surface mixed layer extends down to the lake bottom, ℓ_{ml}, shown in figure 3(*c*).

From the cross-shore discharge, one can estimate an essential quantity, the flushing time scale of the littoral zone:

$$\tau_F = \frac{V_l}{q}. \tag{5.4}$$

If the volume geometry (per unit width) V_l can be described through an analytical expression or approximation, we can utilise scaling relationships for the cross-shore transport, such as those outlined in (5.2) and (5.3), to derive a reduced expression for the flushing time scale τ_F. This parameter provides crucial insights into the pace at which semi-enclosed waters undergo renewal. It is a fundamental metric for characterising the residence time of water constituents in a region and gauging the overall functionality of water bodies (Monsen *et al.* 2002).

Recent field observations (Doda *et al.* 2022, figure 9) and numerical experiments (Ulloa *et al.* 2022) provide robust confirmation of laboratory findings and theoretical scaling (Sturman & Ivey 1998), establishing proportionality coefficients c_u and c_q between 1/3 and 0.35. Field observations of the unit-width discharge were collected within the sloping zone. In contrast, numerical experiments estimated the discharge at the transition from the plateau zone (P) to the sloping zone (s), schematised in figure 3(*c*) ($x = \ell_p$). At this specific region, Ulloa *et al.* (2022) proposed that the buoyancy-driven cross-shore transport scales as

$$q_P = (0.35 \pm 0.05) d (B_0 \ell_p)^{1/3}, \tag{5.5}$$

with $c_q \approx 0.35 \pm 0.05$ and $(B_0\ell_p)^{1/3}$ representing the Phillips (1966) velocity scale. Although the precise explanation for c_q remains elusive, their consistent validation across diverse scenarios underscores their significance. This scaling framework proves instrumental in addressing the question of TS seasonality. In the investigation by Doda *et al.* (2022), it was observed that TS exhibit boosted intensity in late summer, marked by increased discharge attributed to larger values of α and, consequently, B_0. Furthermore, the process extends over a more prolonged duration during winter, shedding light on the temporal dynamics of TS occurrences.

https://doi.org/10.1017/flo.2024.31 Published online by Cambridge University Press

6. Unsteady forcing

6.1. Studies considering periodic thermal forcing

Motivated by the diurnal cycle of TS outlined by Monismith *et al.* (1990), Farrow & Patterson (1993) developed a linear model incorporating a simple diurnal heat flux cycle. This model aimed to capture both the cooling and heating phases within a fluid body characterised by uniform and small slopes. In this idealised representation, the heat source and sink were vertically distributed across the water column with varying depths, establishing a horizontal density gradient that drove phases of differential heating and cooling over a diurnal cycle. The authors derived analytical expressions for the velocity field and asymptotic solutions, delineating the diffusive regime observed in shallow waters and the inertial regime observed in deeper waters (Mao *et al.* 2009). Their findings were validated through fully nonlinear numerical simulations conducted under weak thermal forcing conditions.

The elegant asymptotic approach pioneered by Farrow & Patterson (1993) in the context of periodically forced sloping water bodies was generalised for systems with gradually varying topography by Farrow (2004). These solutions were subsequently extended to encompass more complex environments and diverse periodic forcing mechanisms by various authors (Bednarz *et al.* 2009*b*; Farrow 2013*b*; Lin & Wu 2014; Lin 2015; Farrow 2016; Ulloa *et al.* 2018; Mao 2019; Mao, Lei & Patterson 2019; Coenen *et al.* 2021). While these models may not capture the complexness of the highly nonlinear dynamics observed in nonlinear simulations, laboratory experiments and field observations, they effectively encapsulate the fundamental features of TS, especially their characteristic diurnal rhythm.

Developing novel experiments, Sturman & Ivey (1998) explored the convective exchange phenomena between shallow and deep basins within a water body due to periodic surface thermal forcing. The authors induced differential heating and cooling in a system where a uniform slope region interconnected a shallow reservoir and a deep reservoir. The results revealed that a destabilising heat flux in the shallow region initiated a vigorous exchange flow between the shallow and deep basins. As in the case of steady surface cooling, the resulting discharge per unit width was proportional to $q_d \sim (B_0\ell_p)^{1/3}d$, where B_0 denotes the destabilising surface buoyancy flux across the horizontal extent ℓ_p of the shallow plateau region with a depth d. In contrast, experiments involving a stabilising surface buoyancy flux within the same shallow plateau region exhibited a discharge per unit width proportional to $q_\delta \sim (B_0\ell_p)^{1/3}\delta$, with $\delta < d$ characterising the thermal boundary layer thickness of the exchange flow.

6.2. Diurnal cycle in the field

In temperate water bodies, atmospheric heat exchange causes a diurnal cycle of daytime heating and night-time cooling, with respective intensities modulated by seasons. In a simplified conceptual model we can consider that the water body uniformly loses heat at a rate $H_{net,0}(t) = H_{Q,0}(t) > 0$ over a given time scale τ_{cool} and gain heat at a varying rate $H_{net,0}(t) < 0$ over the rest of the day τ_{warm}, as can be seen, for instance, with the hourly resolved heat flux measurements in Doda *et al.* (2022). These two phases define the cooling–heating diurnal cycle. For a sloping topography, each phase is associated with the formation of lateral temperature gradients: the cooling–heating diurnal cycle generates a differential cooling–heating cycle with some inertia (Monismith *et al.* 1990; James *et al.* 1994).

Recent measurements in a wind-sheltered elongated lake (Doda *et al.* 2022) highlighted how forcing conditions affect the formation and destruction of TS over a diurnal cycle during the summertime period (figure 8). The net surface buoyancy flux $B_{net,0}$ ranged from $-2 \times 10^{-7}\,\mathrm{W\,kg^{-1}}$ during the daytime to $1 \times 10^{-7}\,\mathrm{W\,kg^{-1}}$ during night time (figure 8*c*), with the change in sign mostly due to the solar radiation during daytime ($B_{SW,0} < 0$). While not shown, the wind remained negligible during and before the period of measurements. The vertical velocity recorded with acoustic Doppler current profilers (ADCPs, all details in Doda *et al.* 2022) confirmed that the net night-time cooling was strong enough to trigger convective mixing, with organised upward and downward plumes reaching vertical velocities of $5\,\mathrm{mm\,s^{-1}}$ (figure 8*d*). Such convective mixing could erode and deepen the daily shallow stratification, as

https://doi.org/10.1017/flo.2024.31 Published online by Cambridge University Press

can be observed with the 0.05 °C isotherm lines gradually becoming vertical (e.g. homogeneous profile) during the first part of the night (figure 8*e*). Interestingly, a cross-shore circulation started 3 h after complete vertical mixing, with a marked downslope flow near the bottom and a weaker opposite flow above (note that the upward-looking ADCP did not resolve the velocity near the surface). An interesting dynamic observed by Doda *et al.* (2023) was the striking vertical oscillations of the interface between the downslope flow and the onshore, with fluid excursion spanning approximately 1–2 m, representing nearly 100 % of the thickness of the TS.

Results reported by Doda *et al.* (2023) showed that, by the end of the cooling phase, the water column along the sloping zone exhibited thermally controlled stratification near the bottom. This increase in water density at the base of the water column was attributed to the persistent flow of colder water downslope. Another striking observation is the intensification of the TS in phase with the weakening of vertical convection at the onset of radiative heating. The cross-shore velocity increased above 2 cm s^{-1} and the induced bottom stratification reached $\partial T/\partial z \sim 0.1$ °C m^{-1} at the beginning of the heating phase. This flushing lasted several hours while radiative heating increased and re-stratified the water column. This example, supported by consistent observations, challenges the traditional assumption that most of the transport due to night cooling occurs at night; instead, it highlights that the primary flushing occurs in the early morning. This underscores the need for a quantitative understanding of physical processes to elucidate the timing, formation and fate of TS. In the next section we delve into a more detailed review of the effects of convective mixing on TS dynamics.

6.3. Two dynamic phases of transport modulated by penetrative convection

Time-varying forcing highlights two contrasted dynamical structures of the TS convective flow (Doda *et al.* 2023). Qualitatively, the first phase is characterised by a weak density current of fluctuating thickness and active free convection taking place in the upper layer. This phase is defined as the convective phase, C phase. The second phase is characterised by an intensification of the density current, a more stable current interface over time and a decay of convection in the upper layer, denoted as the relaxation phase, R phase. These two distinctive regimes are schematised in figure 10(*a*).

The lower limb observed during the C phase is characteristic of a density current propagating in an active turbulent environment. Such a density current does not follow established scaling. The propagation of density currents under turbulent background conditions has been studied in the laboratory (Linden & Simpson 1986; Simpson 1986). The findings of these laboratory experiments are supported by recent field experiments (Doda *et al.* 2023), showing that turbulence in the convective upper layer eroded the stratified downslope flow. This process is similar to the case of a uniform destabilising buoyancy flux competing with a local buoyancy flux that produces a stable density stratification (Wells, Griffiths & Turner 1999). The convective Richardson number, Ri_c, presented in (E1*a–c*) is a convenient non-dimensional number to evaluate how convective plumes impinging at density interfaces alter the stratified flow (Baines 1975; Noh, Fernando & Ching 1992; Cotel & Kudo 2008). Here Ri_c is a measure of the relative intensity of penetrative convection with respect to the stratified downslope flow. Below a critical value of $Ri_c^{(crit)} \approx 10$, convective plumes can penetrate across the stratified layer (Noh *et al.* 1992; Cotel & Kudo 2008). The penetration depth of convective plumes can be defined as

$$\delta_c = \frac{|w_c|}{N_d}, \tag{6.1}$$

where N_d is the depth-averaged buoyancy frequency within the gravity current. The dominant role of convection over shear-driven disturbance across the current interface can be assessed by comparing δ_c with the thickness of the shear (δ_S) and density (δ_ρ) interfaces (Zhu & Lawrence 2001): $\delta_S = (U_d - U_a)/(\partial u/\partial z)_{max}$ and $\delta_\rho = (\rho_d - \rho_a)/(\partial \rho/\partial z)_{max}$. Indices d and a refer to the density current and the ambient fluid, respectively.

https://doi.org/10.1017/flo.2024.31 Published online by Cambridge University Press

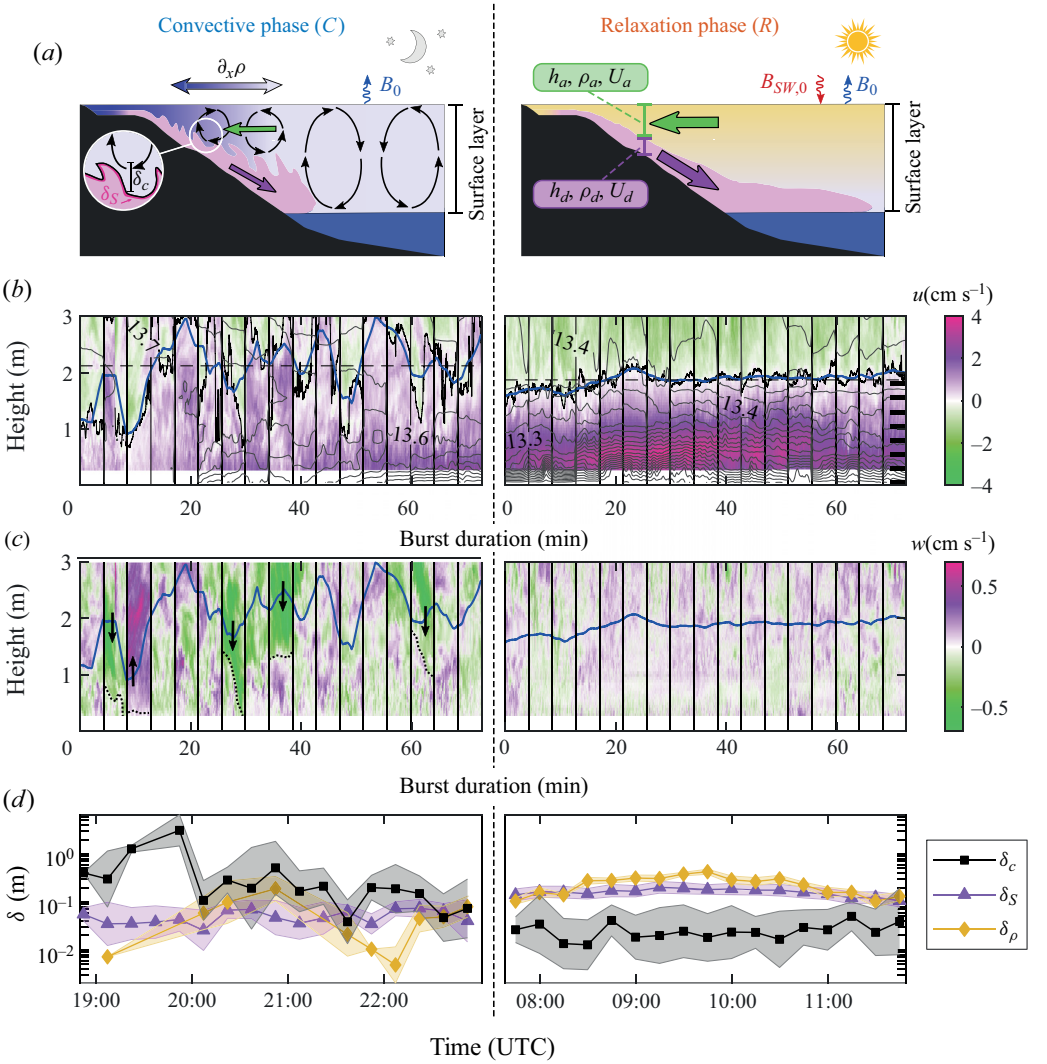

Figure 10. *Subsets of the convective and relaxation phases captured in the sloping region on 6–7 November 2019 in Rotsee with schematics of the processes in (a). (b) High frequency cross-shore velocity above the sediment. Solid black and blue lines depict the high frequencyand smoothed upper interface of the gravity current, respectively. The dashed horizontal line indicates the average thickness* $\overline{h_d}$*. Grey lines are* $0.02\,^{\circ}C$ *isotherms and numbers refer to temperatures. (c) Same as (b) for the vertical velocity. Arrows highlight strong convective downdrafts and updrafts penetrating across the interface. (d) Burst-averaged time series of penetrative length scale* δ_c*, shear interface thickness* δ_S *and density interface thickness* δ_ρ *with standard deviation indicated with the shaded colours. Adapted from Doda et al. (2023).*

The driving processes responsible for the distinct dynamics of the two phases can be retrieved from a statistical description of Ri_c, δ_c, δ_S and δ_ρ. The C phase is characterised by $\delta_c > \delta_S, \delta_\rho$, suggesting that convective plumes penetrate beyond the current interface defined from shear and density and erode the stratified layer (figure 10). Furthermore, Ri_c increased from values close to $Ri_c^{(crit)}$ during the C phase to orders of magnitude larger, confirming that the TS dynamics depend on the interaction between penetrative convection and the gravity currents. The enhancement of vertical fluxes

https://doi.org/10.1017/flo.2024.31 Published online by Cambridge University Press

between the downslope flow and the ambient layer by convective mixing diluted transported tracers and diminished the cross-shore exchange during the C phase. A similar reduction in the lateral transport of tracers due to turbulent diffusion has been reported for exchange flows (Helfrich 1995; Winters & Seim 2000; Hogg, Ivey & Winters 2001). Linden & Simpson (1986) observed that the flow became vertically mixed after a distance L_x. In the case of penetrative convection, this distance represents how far the gravity current propagates before being entirely eroded by penetrative plumes and can be defined as $L_x \sim U_s h_d / w_e$, where $w_e = A w_c / Ri_c = A B_0 h_m / (g' h_d)$ is the convective entrainment velocity, with A an empirical coefficient (Deardorff, Willis & Stockton 1980). Considering the presented case of Lake Rotsee, a numerical example is given with $g' \sim g(\partial\rho/\partial x)\Delta x/\rho_0 \approx 4 \times 10^{-4}\,\mathrm{m\,s^{-2}}$, $h_d \approx h_m \approx 2\,\mathrm{m}$, $B_0 \approx 1 \times 10^{-7}\,\mathrm{W\,kg^{-1}}$ and $A \approx 0.2$ (Sullivan *et al.* 1998), and we retrieve $L_x \approx 0.5 g'^{3/2} h_l^{1/2} h_d^2 / (A B_0 h_m) \approx 700\,\mathrm{m}$, which is consistent with observations of complete mixing (Doda *et al.* 2023). Such a degeneration of the downslope stratified layer before reaching the lake interior confirms the numerical results by Ulloa *et al.* (2022) during the C phase. In these numerical experiments and in Rotsee, the deep stratified region represents a larger portion of the surface area compared with the shallow littoral region such that the ratio of deep to shallow length scales defined in Wells & Sherman (2001) is $\mathcal{R} = \ell_{deep}/\ell_{shallow} = (\ell_{basin} - \ell_p - 0.5\ell_s)/(\ell_p + 0.5\ell_s) > 1$, where ℓ_{basin} is the distance from the shore to the deepest point. From laboratory experiments reaching steady state, Wells & Sherman (2001) found that the stratified layer induced by the gravity current is reduced for $\mathcal{R} > 1$, which is consistent with the observed erosion of the downslope flow in Ulloa *et al.* (2022) and Doda *et al.* (2023). Yet, the role of the basin topography in the competition between TS and penetrative convection in the field requires further research.

The transition from the C phase to the R phase occurred at sunrise when the net cooling heat flux diminished and the intensity of convection weakened. This caused a sudden drop of $|(\partial\rho/\partial x)|$ and a baroclinic adjustment with an intensification of the downslope gravity current. The maximal cross-shore transport was observed during the R phase in Lake Rotsee (Doda *et al.* 2022), in agreement with numerical simulations of TS (Chubarenko *et al.* 2013; Safaie, Pawlak & Davis 2022). This relaxation is comparable to the frontogenesis observed by Linden & Simpson (1986) once turbulence was turned off. The intensification of gravity currents with weaker turbulent mixing has also been observed in the atmosphere (Simpson, Mansfield & Milford 1977; Sha, Kawamura & Ueda 1991; Parker *et al.* 2005) and estuaries (Hetzel *et al.* 2015). In this R phase, the averaged downslope velocity $U_d \approx 1.5 \pm 0.4\,\mathrm{cm\,s^{-1}} \approx 0.9 U_s$ matched the velocity scale based on horizontal density gradients in a quiescent environment $U_s \sim 0.5\sqrt{g h_l \Delta\rho/\rho_0}$, where $\Delta\rho$ is the lateral density difference between shallow and deep regions and $\rho_0 = 1000\,\mathrm{kg\,m^{-3}}$ is the reference density. In the presence of convection during the C phase, however, it was only $U_d \approx 0.8 \pm 0.3\,\mathrm{cm\,s^{-1}} \approx 0.5 U_s$. This observation is consistent with Linden & Simpson (1986) who demonstrated that the front velocity of lock-exchange gravity currents in turbulent conditions was less than the velocity scale U_s.

In addition to modifying the flow dynamics, penetrative convection also affects the growth of the gravity current by changing the amount of ambient water entrained into the downslope flow. The net shear entrainment coefficient is expressed as $E_{net} = (\partial/\partial x)(U_d h_d/(U_d - U_a))$, where U_d and h_d are the depth-averaged velocity and thickness of the downslope flow, respectively, and U_a is the depth-averaged velocity in the ambient layer. Here E_{net} has been parameterised as a function of the bulk Richardson number $Ri_B = g' h_d \cos\theta/(U_d - U_a)^2$ in quiescent environments, where θ is the bottom slope angle (Ellison & Turner 1959; Cenedese & Adduce 2010). The effect of convective plumes on E_{net} is not well understood. Fer *et al.* (2002*b*) reported higher E_{net} in TS interacting with convective plumes compared with the parametrisation of Ellison & Turner (1959), but their estimated E_{net} was lower than expected from the large Reynolds number $Re = U_d h_d/\nu \approx 10^5$ (Cenedese & Adduce 2010). The contribution of convective plumes to E_{net} could be examined in the field from simultaneous velocity measurements along a cross-shore transect. The effects of the return flow U_a on the entrainment must be included since $h_d/h_a \approx 1$, as in counterflows (Moore & Long 1971; Christodoulou 1986).

https://doi.org/10.1017/flo.2024.31 Published online by Cambridge University Press

7. Fate

7.1. Intrusion in the thermocline

Thermal siphons contribute to transporting dissolved gases and compounds, modifying the lake ecosystem dynamics. These convective flows are often viewed as facilitators of deep oxygen ventilation and mixing with density currents flowing underneath the thermocline. Yet, for a TS to penetrate the thermocline, the initial horizontal temperature difference between littoral and surface pelagic waters (ΔT_x) must be greater than the vertical temperature difference in the vicinity of the thermocline (ΔT_z). Knowing the characteristics of the basin and the thermal stratification, and assuming that (i) the build-up of the horizontal temperature gradient (see § 4) is faster than the flushing time scale τ_F (5.4) and (ii) neglecting any entrainment, it is possible to estimate the buoyancy flux needed over the flushing time scale period to generate such underflow. From (4.9), the horizontal temperature difference that drives TS is

$$\Delta T_x(t) = \frac{B_0}{g\alpha d}\left(1 - \frac{d}{h_m}\right)t. \tag{7.1}$$

The condition for the TS to generate an underflow is that $\Delta T_z < \Delta T_x$. At $t = \tau_F$, it yields

$$\Delta T_z < \Delta T_x = \frac{B_0}{g\alpha d}\left(1 - \frac{d}{h_m}\right)\frac{\ell_l}{c_q(B_0\ell_{ml})^{1/3}}. \tag{7.2}$$

For a deep thermocline, $d/h_m \ll 1$ and $\ell_l \approx \ell_{ml}$, the previous inequality reduces to $\Delta T_z < (B_0\ell_{ml})^{2/3}/c_q g\alpha d$.

Numerical applications with $B_0 = O(10^{-7})\,\mathrm{m^2\,s^{-3}}$, $d = 10\,\mathrm{m}$, $\ell_{ml} = 1000\,\mathrm{m}$ and $\alpha \sim 10^{-4}\,^\circ\mathrm{C}^{-1}$ suggest that ΔT_z should be smaller than $\Delta T_x \approx O(10^{-2})\,^\circ\mathrm{C}$, meaning that the interior basin should be nearly well mixed. Therefore, TS are unlikely to penetrate beneath the thermocline or to lead to density current splitting at the thermocline as observed in Cortés *et al.* (2014). From our perspective, other processes must coexist with TS to facilitate such deep ventilation from lateral boundaries (see, for instance, Reiss, Lemmin & Barry 2022; Peng *et al.* 2024). Future research should explore the interplay of complex bathymetric features, including sills, with wind and destabilising heat fluxes. This topic falls into the category of interbasin exchanges and is not discussed here. Another intriguing finding was reported by Wells & Sherman (2001) through a combination of laboratory experiments and theoretical considerations. The authors suggested that, under specific bathymetric conditions (see figure 5), TS can sustain a winter stratification in the deep basin from initially fully mixed conditions. This phenomenon may occur when (i) the ratio between the deeper and shallower areas of the lake is less than 1 and (ii) the ratio between shallow depth and deep depth is less than 0.5, resulting in the development of a surface mixing layer and a stratified deep region. These results challenge the long-standing view that deep lakes (e.g. here taken as water depths larger than the direct vertical extent of mixing by wind energy) can be fully mixed. Instead, as long as the lake has significant shallow areas (i.e. $h_{mean} \ll h_{max}$), TS prevent full vertical mixing induced by destabilising surface cooling by maintaining a weak bottom stratification. Detailed conductivity, temperature and oxygen profiles could reveal fine-scale structures in the deep water associated with such processes and facilitate progress in this research area.

While reaching the conditions for underflow from TS seems unlikely to be achieved in the field, the intrusion of the thermally driven density current into the thermocline can be identified from temperature and current profiles (figure 11). Doda *et al.* (2024) followed the path of natural dissolved oxygen and krypton injected at the shore with portable mass spectrometers. The authors showed that the peaks in krypton and dissolved oxygen matched the timing and depth of the observed peak in velocity in the thermocline region. Similar approaches for river intrusion can be used to infer the pathway of the density currents (Cortés *et al.* 2014), the interaction with the water body (Ramón *et al.* 2020) and the length scale over which the intrusion diffuses into the background fluid (Hogg *et al.* 2013).

https://doi.org/10.1017/flo.2024.31 Published online by Cambridge University Press

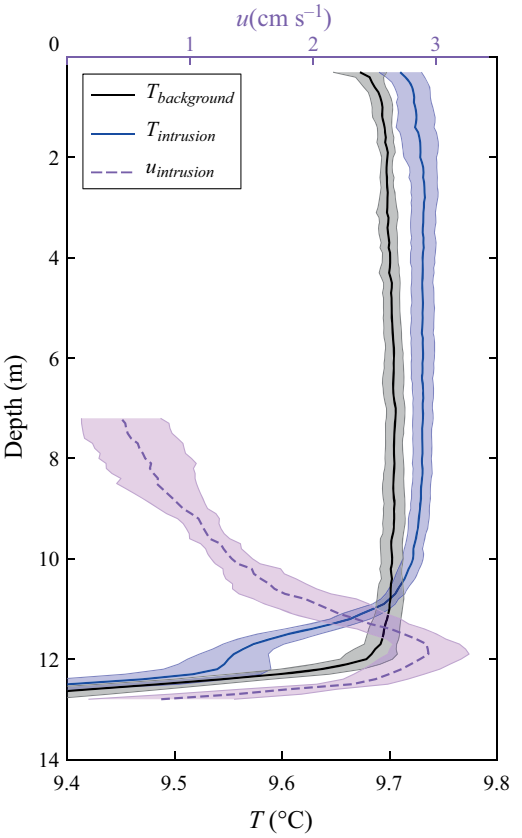

Figure 11. *Temporally averaged profiles of temperature (blue) and cross-shore velocity (pink) in the TS intrusion region in Rotsee (~600 m from the shore). The background averaged temperature profile collected at the lake centre (~1 km from the shore) is shown in black. Shaded areas depict the standard deviation. The intrusion creates a cold layer at the base of the mixed layer that is not observed at the lake centre. Adapted from Doda et al. (2024).*

7.2. Large-scale circulation induced by TS: Observations from ice-covered lakes

Thermal siphons challenge the one-dimensional view of lakes' dynamics with the interaction between bathymetry and surface heat fluxes driving dense water into the deeper basin. However, isolating this source of heat and momentum proves challenging amidst the multitude of processes acting on lakes. An efficient way to investigate the large-scale effect of TS on lakes is to look at ice-covered lakes where wind-driven kinetic energy is largely halted, providing an opportunity to isolate buoyancy-driven processes. Studying ice-covered freshwater lakes corresponds to transitioning to the opposite side of the T_{md}, where the equation of state now links an increase in temperature to a rise in density. In late winter, also known as the winter II phase (Kirillin *et al.* 2012), a diurnal cycle of penetrative radiative heating surpasses diffusive cooling at the ice–water interface, resulting in a net loss of buoyancy. This triggers both penetrative turbulent convection (Farmer 1975; Kirillin *et al.* 2012; Yang *et al.* 2017; Bouffard *et al.* 2019) and downslope gravity currents, the latter stemming from differential heating in the shallows (Kenney 1996; Stefanovic & Stefan 2002; Salonen *et al.* 2014; Kirillin *et al.* 2015; Ulloa *et al.* 2019; Cortés & MacIntyre 2020).

Beneath the ice, the heating and deepening of the convective mixed layer are conventionally viewed as a one-dimensional vertical process (Farmer 1975; Mironov *et al.* 2002). Often, the role of lateral heat advection caused by gravity currents is disregarded. However, field evidence suggests the importance of

https://doi.org/10.1017/flo.2024.31 Published online by Cambridge University Press

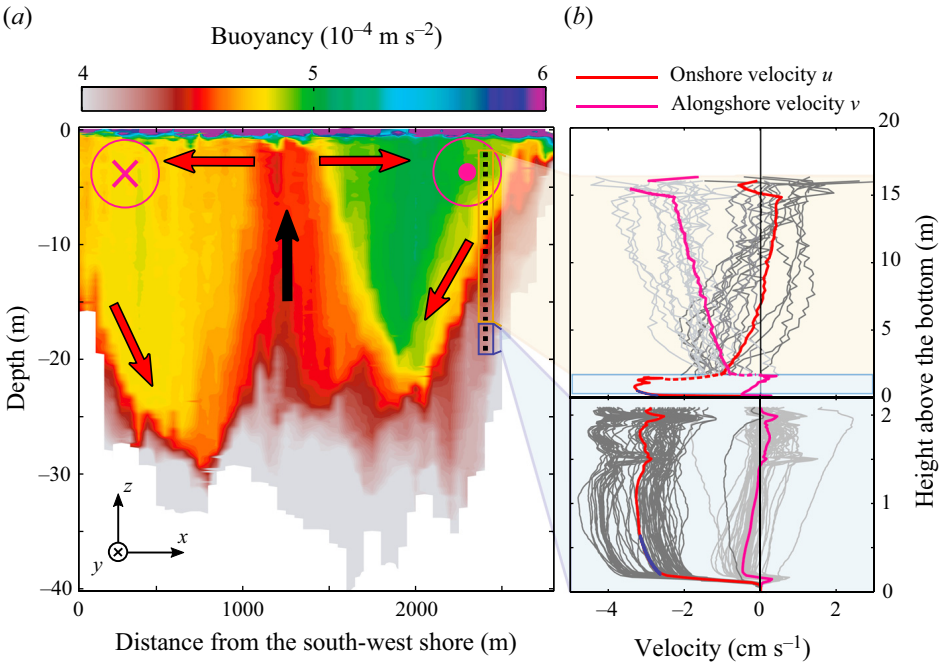

Figure 12. *(a) Buoyancy distribution based on a transect of conductivity–temperature–depth (CTD) profiles with the approximate position of the two current velocity recorders relative to the lakeshore and their vertical coverage marked by the thick dotted line and thin coloured rectangles, respectively. The red and black arrows depict the cross-shore circulation and the central upwelling, respectively. The surface anticyclonic gyre is shown by the pink circles. (b) Combined individual (grey lines) and time-averaged (red and pink lines) vertical profiles for the onshore and alongshore velocity components collected with standard (top) and high-resolution (bottom) ADCPs. The blue line marks the logarithmic fit of the onshore velocity component. Adapted from Kirillin et al. (2015).*

such lateral flows. For example, Kirillin *et al.* (2015) observed an axisymmetric basin-scale circulation in the ice-covered arctic Lake Kilpisjärvian, driven by heat flux from the shallow region. They notably identified a dense underflow creating upwelling at the lake centre (figure 12).

Through numerical investigation of the energy and heat balance of radiatively driven under-ice convection, Ulloa *et al.* (2019) quantified the role of lateral flows and their impact on the evolution of the diurnally active convective mixed layer. They demonstrated that a heat balance can be employed to assess the rate of mixed-layer warming and that neglecting differential heating and lateral fluxes would lead to an underestimation of this rate (figure 13). The heat balance in an interior volume $\tilde{\mathrm{V}}$, shaded as a blue area in figure 13(*a*), extending from the water–ice interface to the depth of the convective mixed layer h_m is

$$\frac{\mathrm{d}T}{\mathrm{d}t} = \frac{1}{h_m}(F_{ext} + F_{adv}), \tag{7.3}$$

where F_{ext} is the sum of the solar heating rate, depicted by the red arrow in figure 13(*a*), and the diffusive heat lost towards the ice, green arrow in figure 13(*a*), and F_{adv} is the summation of advective heat fluxes across the lateral and bottom boundaries of the control volume, shown in yellow arrows in figure 13(*a*). Essentially, F_{adv} accounts for the contribution of lateral heat transport from the shallows to the heating of the lake interior. Ulloa *et al.* (2019) demonstrated that the relative importance of the advective term F_{adv} (differential heating) in comparison to the one-dimensional effects of radiative heating and diffusive cooling at the ice–water interface is geometrically controlled, and can be estimated *a priori* for any lake

https://doi.org/10.1017/flo.2024.31 Published online by Cambridge University Press

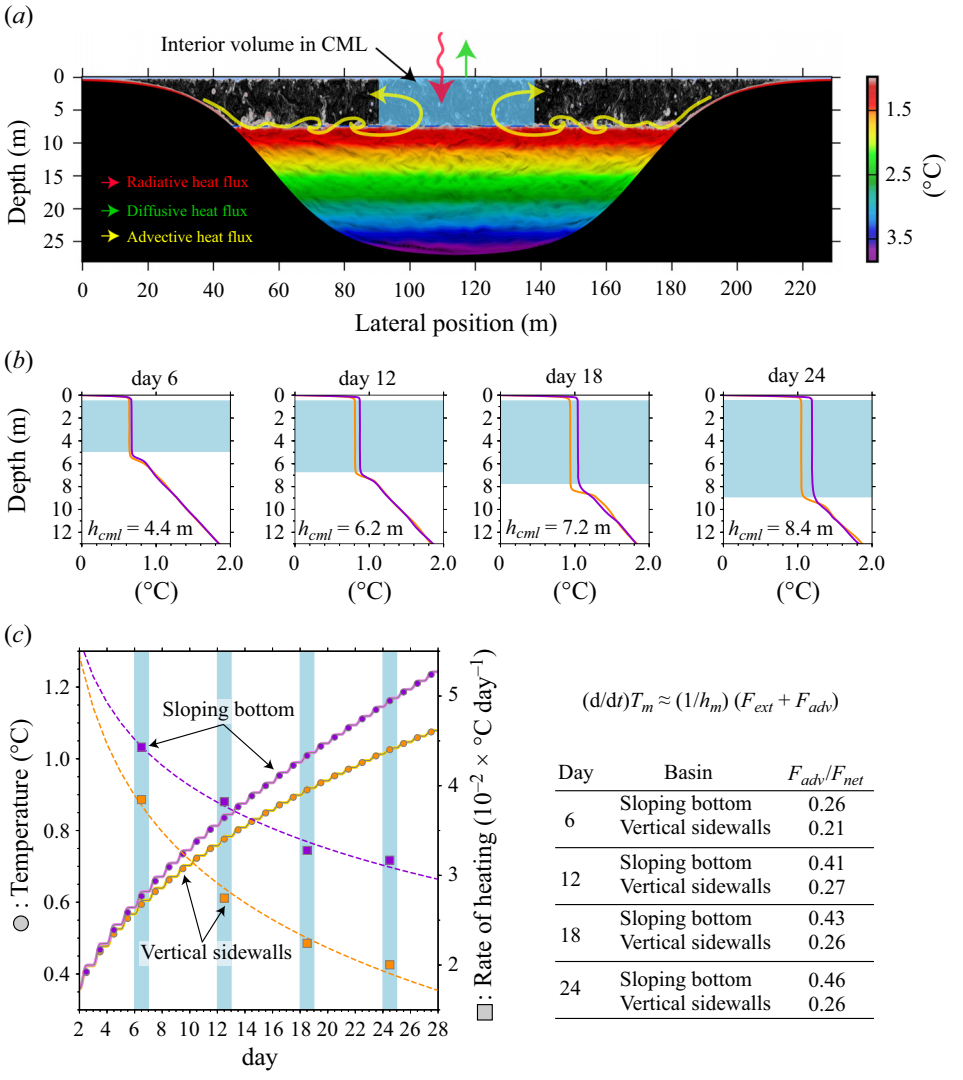

Day	Basin	F_{adv}/F_{net}
6	Sloping bottom	0.26
	Vertical sidewalls	0.21
12	Sloping bottom	0.41
	Vertical sidewalls	0.27
18	Sloping bottom	0.43
	Vertical sidewalls	0.26
24	Sloping bottom	0.46
	Vertical sidewalls	0.26

Figure 13. *(a) Control volume (blue shading) for interior heat balance using (7.3). (b) Laterally averaged, midday temperature profiles for basins with a sloping bottom (purple) and vertical sidewalls (orange). (c) Temperature in the interior of the convective mixed layer (left axis, circles) and net daily averaged heating rate (right axis, squares). (d) Ratio of daily averaged heat fluxes for the days shown in (b). Adapted from Ulloa et al. (2019).*

morphology, incorporating a shallow zone correction to the one-dimensional mixed-layer heat balance. In relative terms, the extent of underestimation of the contribution of advection to the one-dimensional estimate of the warming of the convective mixed layer can be quantified by the geometrical factor G:

$$G = \gamma \left(\frac{\bar{h}}{h_m} - 1 \right). \tag{7.4}$$

Here $\bar{h}$ is the average depth of the shallow regions, referring to locations where the basin depth is shallower than the current mixed-layer depth h_m; and γ is the shallow area fraction (= A_s/A_0), where A_0 is the total lake surface area and A_s is the surface area of the shallow regions. Since G consistently

https://doi.org/10.1017/flo.2024.31 Published online by Cambridge University Press

remains lower than 0 in the presence of shallows, a one-dimensional estimate of mixed-layer warming is therefore always an underestimate. This factor underscores the significance of both the shallow area fraction and its mean depth relative to the mixed-layer depth in the lake's interior. Lakes with small values of γ deliver relatively little heat from the shallows to the interior, resulting in minimal impact on the overall mixed-layer evolution due to lateral transport. For a given shallow area fraction, a greater relative mean depth of the shallows results in a reduced lateral temperature contrast and a proportionally smaller effect on the heating of the lake's interior.

The low speed of horizontal flows and the typically high latitude of ice-covered lakes call for low Rossby numbers $Ro = U_h f^{-1} L^{-1}$, where f is the Coriolis frequency and U_h and L are the characteristic velocity and length scales of the flow. This characteristic allows us to assess how the lateral transport of heat initially constrained by lake bathymetry is also modulated by the Earth's rotation. Ramón *et al.* (2021) conducted a set of high-resolution simulations of a bowl-shaped lake under different Rossby numbers to evaluate how the dynamic response depends on lake size and latitude and is ultimately controlled by the Rossby number (figure 14). The latter was defined as $Ro = U/(fR)$, where R is the surface radius of the bowl-shaped lake. In the ageostrophic limit ($Ro = O(10^{-1})$ in figure 14), horizontal density gradients drive cross-shore circulation that transports excess heat to the lake interior, accelerating the under-ice warming there. In the geostrophic regime ($Ro = O(10^{-3} - 10^{-2})$ in figure 14), the circulation of the nearshore and offshore waters decouples, and excess heat is retained in the shallows. The flow regime controls the fate of this excess heat and its contribution to water-induced ice melt. Ramón *et al.* (2021) proposed a modification of the geometrical factor G that accounts for the Earth's rotation, which for a lake with circular surface area and radius R could be simplified to

$$G_{Ro} = \left(1 - \frac{(R - \ell_{ml})^2}{(R - \ell_{ml} + Ro_R)^2}\right)\left(\frac{h_{Ro}}{h_m} - 1\right), \tag{7.5}$$

where Ro_R is the Rossby radius ($Ro \cdot R$) and h_{Ro} is the average depth of the littoral region within a distance Ro_R from the lake interior. Note that for $Ro_R \geq \ell_{ml}$, $G_{Ro} = G$. Differential heating and the Earth's rotation also set up a circulation characterised by the formation of gyres within the convective mixed layer (figure 14). Under-ice gyre circulation has been also reported from field studies (Likens & Ragotzkie 1966; Forrest *et al.* 2013; Kirillin *et al.* 2015). For example, Kirillin *et al.* (2015) observed that the return flow of the axisymmetric basin-scale circulation in the ice-covered arctic Lake Kilpisjärvian turned into a lake-wide anticyclonic gyre, achieving velocities of up to $4\,\mathrm{cm\,s^{-1}}$ (figure 12). Coriolis effects on TS, as exemplified for ice-covered lakes in this section, have also been reported during winter cooling in large lakes at times of $T > T_{md}$. Fer *et al.* (2001), for example, demonstrated that the cross-shore downward current turned into a cyclonic current in Lake Geneva. If we define a Ro number for the littoral region as $Ro = U/(f\ell_{ml})$, low Ro numbers are expected in the littoral regions of large lakes such as the Great Lakes, given their latitudinal location and particularly the extent of these regions ($\ell_{ml}O(10)$ km). An example of the Earth's rotation interacting with differential cooling/heating in such lakes is the formation of the spring and autumn thermal bars.

7.3. Thermal bar

A particularly interesting convective phenomenon, mediated by the nonlinear equation of state of water, occurs in the sloping waters of lakes whose water temperature drops below T_{md}, such as those that freeze seasonally. As autumn progresses and nearshore waters cool faster than deeper waters (differential cooling), the very nearshore region reaches temperatures below T_{md}, creating what is known as the 'thermal bar' (Forel 1880): a transition zone characterised by having a well-mixed water column at T_{md}, from where a downwelling convective flow fosters the formation of two cross-shore convective cells with opposing circulation – which inhibit the exchange between onshore and offshore waters, with potential impacts in the ecological functioning of aquatic systems, as discussed by Holland & Kay (2003) and Terzhevik (2012). As the surface water cooling progresses, the cross-shore position of the thermal bar

https://doi.org/10.1017/flo.2024.31 Published online by Cambridge University Press

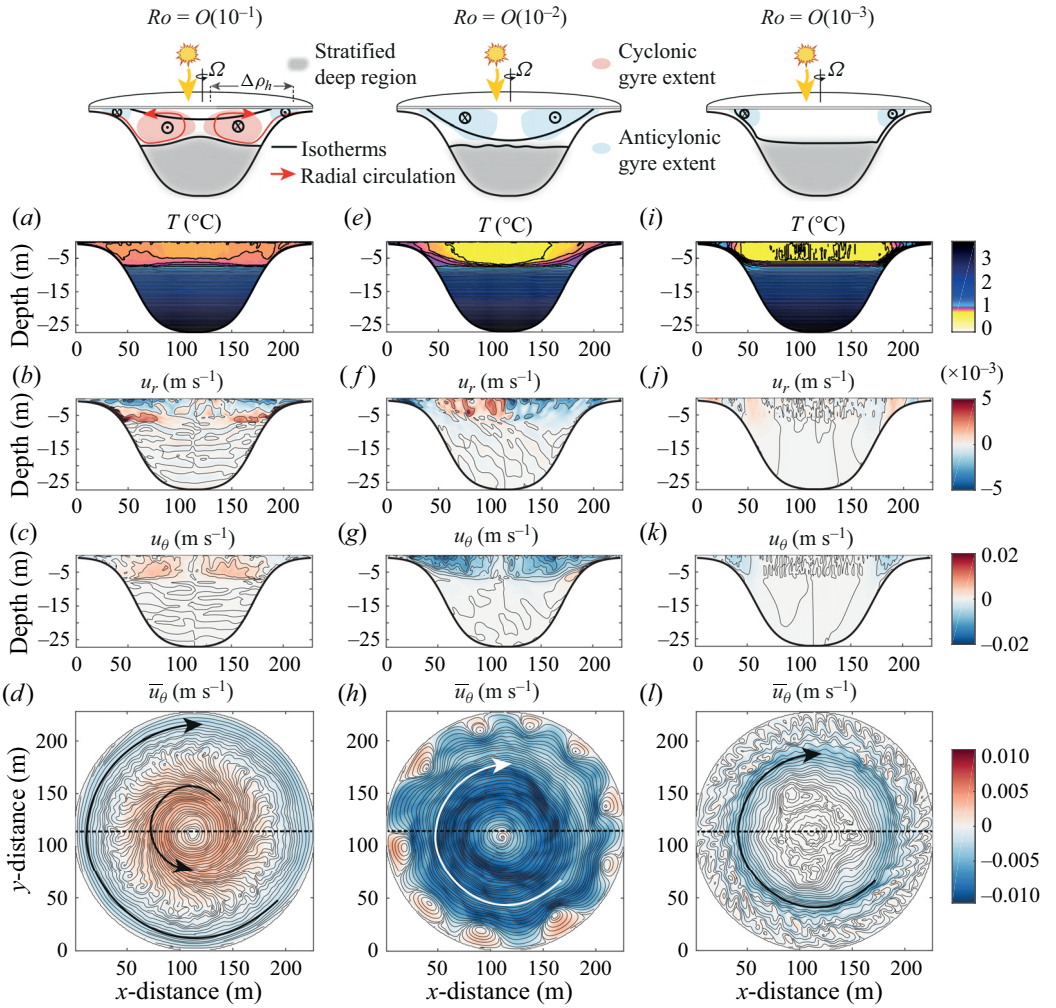

Figure 14. *Snapshots of the thermal and velocity structure for different Ro showing the simulated cross-sectional (a,e,i) temperature (0.02 °C isotherm spacing) and (b,f,j) radial and (c,g,k) azimuthal velocities (0.002 m s^{-1} isovel spacing) and depth-averaged (d,h,l) azimuthal velocities and flow streamlines at* depths $< h_m$. *Radial and azimuthal velocities are positive towards the lake interior and for cyclonic circulation, respectively. Black dashed lines in (d,h,l) show the location of the cross-section displayed in (a–c), (e–g) and (i–k). Results for runs with (a–d) Ro $O(10^{-1})$, (e–h) Ro $O(10^{-2})$ and (i–l) Ro $O(10^{-3})$. Sketches on top conceptualise the under-ice circulation induced by differential heating for the ageostrophic and geostrophic regimes. Adapted from Ramón et al. (2021).*

moves offshore. The same phenomenon emerges during spring. This time, nearshore waters warm faster than deeper water (differential heating), pushing the thermal bar offshore (see schematic in figure 2). The autumn thermal bar has been reported to be difficult to detect given the small temperature gradient between onshore and offshore regions and atmospheric instability (e.g. Huang 1972). The spring thermal bar, however, could last for 1 month (e.g. Boyce *et al.* 1989) and the evolution can be tracked by satellite.

Zilitinkevich, Kreiman & Terzhevik (1992) proposed a scaling for the horizontal displacement rate of the thermal bar following a heat balance approach where the propagation speed is estimated as $H_{net,0}/(\bar{s}\rho C_p(T_{md} - T_0))$, with $\bar{s}$ being the bottom slope and T_0 the initial lake temperature. Following Malm *et al.* (1993) observations on Lake Ladoga, the typical propagation rate is about 2 km day^{-1}

https://doi.org/10.1017/flo.2024.31 Published online by Cambridge University Press

(using $\bar{s} = 10^{-3}$, $H_{net,0} = 200\,\mathrm{W\,m^{-2}}$ and $T_0 = 2\,^{\circ}\mathrm{C}$). Various model approaches have been developed to investigate the circulation induced by the thermal bar, gradually increasing in complexity (Tsydenov 2018, 2019). These range from a steady-state temperature and circulation model that includes the Coriolis effect (Huang 1972), to asymptotic unsteady models (Brooks & Lick 1972; Farrow 1995*a*,*b*; Farrow & McDonald 2002; Farrow 2013*a*) and 2-D hydrodynamic models that incorporate wind stress (Malm 1995). Moreover, we note that other local processes, such as rivers entering lakes, can also trigger a local riverine thermal bar (e.g. Carmack *et al.* 1979). Lastly, we acknowledge that a significant number of studies in thermal bar dynamics were led by the scientist A.I. Tikhomirov between the 50's and 80's; a list of his papers written in Russian are listed in Terzhevik (2012).

8. Wind and differential cooling

The scaling formulae derived from laboratory and theoretical studies (5.1)–(5.4) assumed that differential cooling is the only forcing driving cross-shore transport in the littoral region of a lake, and indeed Doda *et al.* (2022) proved that these equations correctly predicted the measured velocities, unit-width discharges and flushing times during negligible wind conditions in lake Rotsee (e.g. figure 9). However, most of the time lake dynamics result from a combination of different forcings, and, for example, the assumption of calm wind conditions (i.e. zero wind stress) is rarely met in nature. Several field and modelling studies have reported that moderate winds (generally $\lesssim 5\,\mathrm{m\,s^{-1}}$) can block or enhance the cross-shore transport driven by TS (Monismith *et al.* 1990; Roget *et al.* 1993; James *et al.* 1994; Sturman *et al.* 1999; Rueda, Moreno-Ostos & Cruz-Pizarro 2007; Molina *et al.* 2014; Woodward *et al.* 2017; Mahjabin, Pattiaratchi & Hetzel 2019). The results of these studies suggested that there is an interaction regime, where both wind and buoyancy forces are equally important in driving the cross-shore circulation. For enclosed stratified basins, subjected to a uniform and steady surface cooling rate and cross-shore winds (wind acting across the littoral region), recent 3-D numerical hydrodynamic RANS simulations (Ramón *et al.* 2022) have shown that this interaction regime can be characterised by a non-dimensionalised Monin–Obukhov length scale χ_{MO} and is delimited to $0.1 \lesssim \chi_{MO} \lesssim 0.5$, with

$$\chi_{MO} = \frac{L_{MO}}{h_m} = \frac{u_*^3}{kB_0h_m} = \frac{u_*^3}{kw_c^3}. \tag{8.1}$$

Here L_{MO} is the Monin–Obukhov length scale ($= u_*^3k^{-1}B_0^{-1}$) and represents the depth scale over which shear dominates over convection in driving the deepening of a surface mixed layer, k ($\approx$0.41) is the von Kármán constant and the surface friction velocity u_* is defined as $u_* = (\tau_{wind}/\rho_0)^{1/2}$ (e.g. Wüest & Lorke 2003), where τ_{wind} is the surface wind shear stress and ρ_0 is a reference water density. Expression (8.1) provides dual information. First, it provides information about the leading vertical mechanism driving the deepening of the surface mixed layer, with $\chi_{MO} > 1$ indicating that wind shear overcomes convection. Second, from (5.1) and the definition of the convective velocity scale w_c ($\sim(B_0h_m)^{1/3}$), the horizontal velocity of TS scales as $U \sim (B_0\ell_{ml})^{1/3} \sim w_c(\ell_{ml}/h_m)^{1/3}$. Thus, $\chi_{MO} \sim u_*^3\ell_{ml}(kU^3h_m)^{-1}$ also provides a quantification of the relative importance of wind in driving the exchange flows in littoral regions subject to surface cooling. For $\chi_{MO} \sim O(1)$, wind-driven flows dominate the cross-shore circulation.

As χ_{MO} departs from ≈ 0 and goes into the interaction regime, (5.2) would fail to predict the magnitude of the cross-shore discharge. Ramón *et al.* (2022) proposed a practical mathematical expression of the form $q_{total} = q_{TS} + q_{wind}$ that accounts for the buoyancy-driven (q_{TS}), (5.2), and wind-driven (q_{wind}) contributions to the net cross-shore discharge in this regime. For a steady cross-shore wind stress over an enclosed stratified basin, recalling the no-slip bottom boundary condition and flow continuity, and assuming a constant vertical viscosity ν_z within the mixed layer and negligible slope effects ($\bar{s} \ll 1$), the associated maximal wind-driven offshore flow scale in the littoral region is $q_{wind} = u_*^2h_m^2(27\nu_z)^{-1}$. The additive (linear) scaling q_{total} improved the prediction of cross-shore discharge in the littoral region of both the elongated trapezoidal bathymetry reproduced in their RANS simulations (figure 15) and the littoral region in Lake Rotsee. Although the mathematical expression defining q_{total} is a step towards

https://doi.org/10.1017/flo.2024.31 Published online by Cambridge University Press

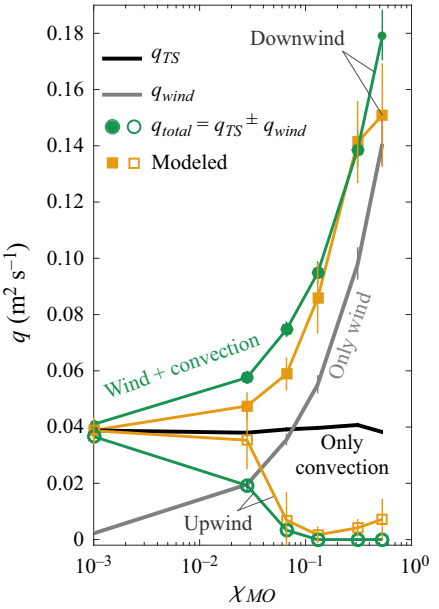

Figure 15. *Time-averaged unit-width discharge predictions with the convective (black), wind-driven (grey) and additive (linear) scaling (green) versus modelled (light orange) unit-width discharge in a profile located upwind (open symbols) and a downwind profile (closed symbols). Vertical lines on the modelled values show ± one standard deviation. Vertical lines in the different scaling curves show the uncertainty coming from the 95 % confidence interval of the fitting coefficient* c_q *(*$= 0.29 \pm 0.006$*) in* (5.2) *and* $\nu_z = 6.06 \times 10^{-4} \pm 3.6 \times 10^{-5}$ m^2 s^{-1}*. 'Downwind' (respectively, 'Upwind') refers to the location of the estimated unit-width discharge on an elongated lake. Adapted from Ramón et al. (2022).*

multi-forcing analysis, the assumed quasi-stationary conditions may not be met in deeper littoral regions, with lower slopes, lower surface buoyancy fluxes and/or shorter cooling periods (e.g. Molina *et al.* 2014), where flow dynamics may follow an inertial–viscous buoyancy balance (e.g. Farrow & Patterson 1993; Farrow 2013*b*; Lin 2015; Ulloa *et al.* 2018). Besides wind stress, strong background currents and/or high bed roughness also contribute to the net cross-shore exchange (Ulloa *et al.* 2018). In addition, alongshore tidally driven (Ulloa *et al.* 2018; Safaie *et al.* 2022) or wind-driven currents (e.g. Lentz & Fewings 2012; Wu, Cahl & Voulgaris 2018; Jabbari *et al.* 2019) could also affect cross-shore flows via Coriolis acceleration.

9. Conclusion, challenges and outlook

The phenomenon of thermally driven cross-shore flows resulting from heat exchange between a sloping water body and the atmosphere is commonly referred to as a TS. In lakes, the manifestation of this process is frequently obscured by the influence of wind and the resulting wind-driven motions within the stratified basin. Nevertheless, TS retain significance, especially during the cooling season in wind-sheltered lakes and in late winter in ice-covered lakes where solar radiation warms the surface water. Due to the initiation time scales and the vertical mixing by free convection in the surface layer, cross-shore transport experiences a temporal shift (see § 4). In the case of diurnal forcing, the flow is observed to penetrate the pelagic zone in the morning. Such a temporal shift should be carefully assessed when investigating biogeochemical processes with diel variability, like primary production.

https://doi.org/10.1017/flo.2024.31 Published online by Cambridge University Press

Thermal siphons underscore the necessity of considering lateral transport and mixing in lakes rather than relying solely on a vertical one-dimensional perspective. Ice-covered lakes serve as compelling field-scale laboratories for investigating subtle processes with well-defined boundary conditions. Thermal siphons in ice-covered lakes not only increase the rate of heating of the surface layer but can also induce basin-scale gyre-type circulation depending on the strength of the forcing, the lake morphology and the latitude (see § 7). The effect of gyre vorticity in intensifying vertical upward/downward transport via the Ekman effect should be further explored in these systems.

Estimating the potential contribution of TS to lake thermodynamics can be straightforward as existing parametrisations rely on external forcing parameters and basin morphology (see § 5). In line with recent studies on vertical heat fluxes, lake stability and internal wave activity (Read *et al.* 2011; de Carvalho Bueno, Bleninger & Lorke 2021), there is a clear opportunity for the interdisciplinary limnology community to benefit from the development of open-source R or Python packages that would provide such *a priori* estimation of the potential and consequences of TS on a given lake. Such tools would greatly assist researchers and practitioners in understanding and predicting the intricate dynamics of buoyancy-driven flows in diverse lake environments.

While the general dynamics is currently well understood, certain processes demand a more thorough investigation. A notable gap exists in our understanding of the entrainment of cross-shore transport during the convective phase (C phase, see § 6.3). The discharge exhibits an increase with propagation distance (Fer *et al.* 2002*b*). This signifies a net entrainment E of ambient water into the gravity current as introduced by Ellison & Turner (1959). The quantification of this entrainment is crucial for determining the intrusion depth of the gravity current under linear stratification conditions (Wells & Nadarajah 2009) and estimating the dilution of transported tracers (Christodoulou 1986). Despite the existence of parametrisations that estimate E based on the bulk Richardson number Ri_b for gravity currents moving into a quiescent environment (Ellison & Turner 1959; Cenedese & Adduce 2010), uncertainty lingers regarding the applicability of these parametrisations to TS during the active C phase. The issue arises from the presence of penetrative convection and the two-way exchange flow that characterises TS. Fer *et al.* (2002*b*) proposed that convective plumes might augment E. However, contrasting results emerge from velocity measurements in Lake Rotsee (Switzerland) and numerical simulations by Ulloa *et al.* (2022), where the computed E is lower than anticipated from Ri_b. These contrasting observations underscore the complexity of estimating entrainment in TS, calling for further investigation through field studies, laboratory experiments and numerical simulations.

In addition, transport parameterisations were systematically derived over the C phase under steady and time-varying forcing conditions. For quasi-steady-state conditions, the magnitude of the coefficient 'c_q' in (5.2) is well constrained, with both numerical and field experiments showing reasonable agreement. Although the value of $c_q \approx 0.35$ strongly suggests that the exchange flow driven by TS might be hydraulically controlled (Farmer & Armi 1986; Finnigan & Ivey 2000), the ultimate nature of this empirical value remains unknown. This encourages further investigation into the internal hydraulics of TS. As a consequence, it is unclear how the 'c_q' coefficient of the scaling '$q = c_q(B_0\ell_l)^{1/3}h_\ell$' might change during the relaxation phase when free convection in the surface mixed layer is rapidly damped (see § 4.8). Recent observations suggest an increase in transport during this phase. However, the particular characteristics of this pulse flow warrant in-depth investigation.

The dynamics of the intrusion of TS at the base of the surface mixed layer also require further investigations to better predict how far TS can propagate and transport dissolved tracers. A detailed quantification of the entrainment, E, during the C phase would determine how the competition between TS and penetrative convection affects their propagation in the pelagic zone. The destruction of the gravity current observed during the C phase in Ulloa *et al.* (2022) and Doda *et al.* (2023) might be specific to the basin topography for which the ratio between deep and shallow areas was greater than 1. If shallow areas dominate, the gravity current could propagate into the pelagic zone during the C phase (Wells & Sherman 2001). The effects of the intrusion on mixed layer deepening and vertical turbulent fluxes could be examined via turbulence measurements.

https://doi.org/10.1017/flo.2024.31 Published online by Cambridge University Press

As introduced in § 1, lakes encompass a multitude of intricate processes. While individual processes are frequently well understood and constrained, the current overarching challenge lies in examining their interplay. Assuming a simplified model of additive (linear) scaling, it is possible to estimate the collective impact of wind and cooling (see § 7). Below, we enumerate additional parameters and processes deserving dedicated attention. Firstly, a comprehensive exploration of the role of sediment heat flux requires an in-depth fluid dynamics investigation. Researchers have observed that the stored heat energy accumulated in the sediment over the summer period is released during the fall and winter period and can instigate cross-shore transport (Zdorovennova 2009; Cortés & MacIntyre 2020), yet a mechanistic model of this process is missing. Secondly, the prevalence of alongshore flows in large lakes demands a closer examination of their interplay with the cross-shore nature of TS. Thirdly, most investigations of TS have solely focused on monotonic changes in bathymetry, either as a wedge case or with a defined plateau region (figure 3). However, it is relevant to recognise that some shallow plateaus are terminated with sills, which will impact the fate of the exchange flows. This particular type of bathymetry should be conceptualised as interbasin exchanges (Finnigan & Ivey 1999; Ivey 2004). Finally, in natural systems the shallow photic zone can host macrophytes. Such vegetation prevents part of the incoming solar radiation from entering into the water body, generally resulting in colder temperature in the vegetation-shaded area compared with the surrounding region. At night, vegetation reduces the surface cooling, resulting in warmer temperatures in the vegetation region. Lövstedt & Bengtsson (2008) observed on Lake Krankesjön (Sweden) an averaged 0.5 °C daytime surface temperature difference between the warmer open water and colder water within the reed belt (average 85 % vegetation occupancy or porosity) that was linked to surface currents (mean 0.8 cm s^{-1}, max 2.3 cm s^{-1}) directed toward the vegetation. Such density currents, including the return bottom following current induced by the horizontal variability in vegetation, were further investigated with asymptotic solutions (using a linear approach with small slopes) in the wedge case (figure 3*a*) by Lin & Wu (2014). They notably showed that the horizontal velocity is significantly reduced by vegetation drag. The horizontal distribution and the density of the vegetation have an important impact on the flow structure. Papaioannou & Prinos (2023) and Prinos & Papaioannou (2024*a*,*b*) used a 2-D model to explore the alternating daily cycles of large-scale circulation patterns under different vegetation densities. Although the flow and transport in the vegetated flat region is an active research area (see, for instance, Zhang & Nepf (2009); Nepf (2012) and references therein), the interaction of vegetation at the sloping boundaries with a TS still need to be fully constrained.

This review deliberately focuses on lakes, yet it is important to conclude by stressing that the significance of TS extends far beyond the realm of inland water bodies. Thermal siphons also influence the fluid dynamics of other aquatic environments, including coastal seas (e.g. Biton, Silverman & Gildor 2008; Grimes, Feddersen & Kumar 2020), coral reef systems (e.g. Monismith *et al.* 2006; Molina *et al.* 2014) and continental shelves (e.g. Ivanov *et al.* 2004). Beyond aquatic environments, TS also share the fluid physics of atmospheric processes such as diurnal land–sea breeze circulation (e.g. Miller *et al.* 2003; Davis *et al.* 2019), urban heat island effect (e.g. Hidalgo, Masson & Gimeno 2010; Wang & Li 2016) and katabatic winds (e.g. El Gdachi *et al.* 2024; Montlaur, Arias & Rojas 2024). Hence, lakes are fascinating systems that serve as excellent natural laboratories for studying and understanding the fluid dynamics of buoyancy-driven flows at field scales.

Appendix A. Surface heat flux

For the purpose of deriving the volume heat budget, in this appendix we consider the reference system at the surface of the water body. Note that the final expressions for surface heat and buoyancy fluxes are independent of the origin of the reference system. The surface heat flux $H_{Q,0}$ (W m^{-2}) results from the combined action of four processes exchanging heat between the atmosphere and the water body: sensible heat exchange, latent heat exchange, incoming and outgoing long-wave radiation (Schmid & Read 2022). Conventionally, positive $H_{Q,0}$ denotes heat being transferred from the water body to the atmosphere (i.e. surface cooling). This surface heat flux acts as a top boundary condition in the energy

https://doi.org/10.1017/flo.2024.31 Published online by Cambridge University Press

equation,

$$H_{Q,0} = -K \left.\frac{\partial T}{\partial z}\right|_{z=z_0}, \tag{A1}$$

where K is the thermal conductivity of water ($\approx 0.6\,\mathrm{W\,m^{-1}\,{}^{\circ}C^{-1}}$ at $T = 20^{\circ}\mathrm{C}$) and $(\partial T/\partial z)|_{z=z_0}$ is the vertical temperature gradient at the water surface. Recall that the bottom boundary condition (at the sediment–water interface) $K(\partial T/\partial z)|_{z=z_b}$ is assumed null.

Short-wave solar radiation is attenuated by absorption and scattering as it penetrates through the water column. The depth-dependent solar radiation heat flux is given by $H_{SW}(z) = H_{SW,0}\exp(k_d z)$ ($\mathrm{W\,m^{-2}}$), where $H_{SW,0}$ ($\mathrm{W\,m^{-2}}$) is the solar radiation reaching the air–water interface or the ice–water interface of the water body, k_d ($\mathrm{m^{-1}}$) is the light attenuation coefficient. This heat flux acts as a volumetric energy source that is conventionally considered negative (in field studies) but it heats up the water body (e.g. Monismith *et al.* 2006; Doda *et al.* 2022).

Therefore, integrating the energy equation ruling the heat budget in an aquatic system of volume V, surface area A_s and mean depth $\bar{D}(= \bar{z}_b < 0)$, the evolution equation for the stored heat is determined by

$$\frac{\mathrm{d}}{\mathrm{d}t}\int_{\Omega} \rho_0 C_p T \,\mathrm{d}\hat{V} = \underbrace{\oint_{\partial\Omega} K\boldsymbol{\nabla} T\cdot\hat{\boldsymbol{n}}|_{z=z_0}\,\mathrm{d}\hat{S}}_{\textit{sensible, latent and long-wave radiation}} + \underbrace{A_s(-H_{SW,0})[1-\exp(k_d\bar{D})]}_{\textit{short-wave radiation}}. \tag{A2}$$

Here, $\mathcal{H} = \int_{\Omega}(\rho_0 C_p T)\,\mathrm{d}\hat{V}$ denotes the net heat in the volume V, C_p is the specific heat of water ($\mathrm{J\,{}^{\circ}C^{-1}\,kg^{-1}}$), ρ_0 is the reference water density and $\hat{\boldsymbol{n}}$ is the outward-pointing normal of the top surface. Assuming that $H_{Q,0}$ in (A1) represents a laterally averaged surface heat flux, the heat balance in (A2) can be expressed simply as

$$\frac{\mathrm{d}\mathcal{H}}{\mathrm{d}t} = -A_s H_{Q,0} - A_s H_{SW,0}[1-\exp(k_d\bar{D})], \tag{A3}$$

where the net heat flux per unit area, including the net short-wave radiation acting at the surface, is (Leppäranta 2015; Schmid & Read 2022)

$$H_{net,0} = H_{Q,0} + H_{SW,0}. \tag{A4}$$

According to field studies convention, the heat content of the water body increases if $H_{net,0} < 0$ (net heating) and decreases if $H_{net,0} > 0$ (net cooling). The surface heat flux changes the potential energy of the water column, which is expressed by a surface buoyancy flux per unit mass $B_0 = \alpha g H_{Q,0}/(\rho_0 C_p)$ ($\mathrm{W\,kg^{-1}}$) (Soloviev & Lukas 2014), where g is the gravitational acceleration ($\mathrm{m\,s^{-2}}$). Surface heat exchange stabilises (stratifies) the water column when $B_0 < 0$ and destabilises it (promoting convection) when $B_0 > 0$. For $T > T_{md}$ ($\alpha > 0$), surface heating stabilises and surface cooling destabilises the water column. The process reverses for $T < T_{md}$ and $\alpha < 0$. Considering the same approximation made in (A4), the net buoyancy flux is

$$B_{net,0} = B_0 + B_{SW,0} = \frac{g\alpha}{\rho_0 C_p} H_{Q,0} + \frac{g\alpha}{\rho_0 C_p} H_{SW,0}, \tag{A5}$$

where $B_{SW,0}$ is the solar radiative buoyancy flux at the surface.

Appendix B. Heat balance during the free convection regime

Here, the heat budget is defined for each of the three zones illustrated in figure 6. Initially, convective motions are laterally localised and vertically confined due to the presence of a physical barrier – either the bottom boundary in zones (P) and (S) or the thermocline in zone (I). Convective plumes diverge

https://doi.org/10.1017/flo.2024.31 Published online by Cambridge University Press

laterally without any specific horizontal preference in the plateau (P) and the interior zone (I). This is not the case in the sloping zone (S), where a portion of the vertical momentum carried down by the thermals transforms into horizontal momentum. However, given the gentle slopes studied in natural systems, of the order of $O(10^{-2})$, such a net transfer from vertical to horizontal momentum remains comparatively weak. Consequently, we assume that the net horizontal heat transport is negligible during regime I; thus, the heat balance can be approximated by

$$\frac{\partial T}{\partial t} + \frac{\partial}{\partial z}(wT) = \frac{\partial}{\partial z}\left(\kappa \frac{\partial T}{\partial z}\right). \tag{B1}$$

We denote the vertical average of a function $\varphi(t, z)$ over a layer h as $\langle\varphi\rangle_{(\cdot)} = h^{-1}\int_h \varphi(t, z)\,\mathrm{d}z$. Here, the subscript $(\cdot)$ represents whether it pertains to zone (P), (S) or (I). Since the water column is well mixed in the vertical in the case of destabilizing forcing, depth-averaging analyses are well justified. Integrating (B1) across the water column d in zone (P) and applying the specified boundary conditions, namely, $w = 0$ at $z = D - d$ and $z = D$, as well as $\kappa(\partial T/\partial z) = -I_0$ at $z = D$ and $\kappa(\partial T/\partial z) = 0$ at $z = D - d$, yields

$$\frac{\mathrm{d}}{\mathrm{d}t}\langle T\rangle_{P)} = -\frac{I_0}{d}. \tag{B2}$$

By integrating (B2) over time, and starting from the initial time $t_0 = 0$, the average temperature within zone (P) changes as follows:

$$\langle T\rangle_{(P)} = \langle T(t_0)\rangle_{(P)} - \frac{I_0}{d}t. \tag{B3}$$

In zone (I) the heat budget considers the combined effect of diffusive and advective fluxes at the base of the convective mixing layer, expressed by the equation

$$\frac{\mathrm{d}}{\mathrm{d}t}\langle T\rangle_{(I)} = -\frac{1}{h_m}\left[I_0 + \left(\kappa\frac{\partial T}{\partial z}\right)\Big|_{z=z_m} + (wT)|_{z=z_m}\right], \tag{B4}$$

where z_m is the height at the base of the surface mixed layer. However, the impact of temperature jump and intensified background stratification tends to substantially reduce the vertical fluxes at the base of the convective layer, as suggested by previous studies (Deardorff, Willis & Lilly 1969; D'Asaro, Winters & Lien 2002). The net heat flux at the base of a convective layer is approximately one order of magnitude smaller than the surface heat flux (Zilitinkevic 1991). To obtain an analytical approximation of $\langle T\rangle_{(I)}(t)$, the balance in (B4) can be simplified to

$$\frac{\mathrm{d}}{\mathrm{d}t}\langle T\rangle_{(I)} \approx -\frac{I_0}{h_m}, \tag{B5}$$

leading to

$$\langle T\rangle_{(I)} \approx \langle T(t_0)\rangle_{(I)} - \frac{I_0}{h_m}t. \tag{B6}$$

In the sloping region (S) the x-dependent depth-averaged temperature evolution, $\langle T\rangle_{(S)}$, follows a similar pattern to (B3) and (B6) but is normalised by the local depth, $D_B(x)$. It is important to note that $\langle T(t_0)\rangle_{(P)} = \langle T(t_0)\rangle_{(S)} = \langle T(t_0)\rangle_{(\mathrm{I})}$. Given our assumption that $T > T_{md}$ and the small temperature drops during the cooling phase throughout the day relative to T_s (approximately 0.1°day-1), we can rely on a local linearization of the equation of state to accurately estimate the density, ρ, and buoyancy, b, for each zone:

$$\frac{\langle\rho\rangle_{(\cdot)}}{\rho_0} - 1 = \alpha(\langle T\rangle_{(\cdot)} - T_0) \quad \text{and} \quad \langle b\rangle_{(\cdot)} = -g\left(\frac{\langle\rho\rangle_{(\cdot)}}{\rho_0} - 1\right) = -g\alpha(\langle T\rangle_{(\cdot)} - T_0). \tag{B7a,b}$$

https://doi.org/10.1017/flo.2024.31 Published online by Cambridge University Press

Appendix C. Vertical momentum balance

Now, let us examine the vertical momentum balance in the initial convective regime, governed by the equation

$$\frac{\partial w}{\partial t} + \boldsymbol{\nabla} \cdot (\boldsymbol{v} w) = -\frac{1}{\rho_0}\frac{\partial p}{\partial z} + b + \nu \nabla^2 w. \tag{C1}$$

Given that free convection regulates vertical momentum transport, meaning the advection of momentum balances buoyancy, we can omit the viscous term $\nu\nabla^2 w$ from (C1). As discussed in Ulloa *et al.* (2022), momentum diffusion $\nu\nabla^2\boldsymbol{v}$ diminishes with higher Rayleigh numbers (Ra). Consequently, for high Ra, $\nu\nabla^2\boldsymbol{v}$ becomes negligible.

By averaging (C1) between the surface at $z = D$ and a height $z \geq D - d$ (denoted by $\langle\cdot\rangle_{D-z}$), and considering negligible variations in vertical velocity during regime I ($\partial\langle w\rangle_{D-z}/\partial t \sim 0$), the vertical momentum balance simplifies to

$$-\left.\frac{w^2}{2}\right|_z \approx -\left(\frac{p_D - p}{\rho_0}\right) + \langle b\rangle_{D-z}(D - z). \tag{C2}$$

Here, p_D and p represent pressures at the surface and a height z, respectively. The balance in (C2) can be expressed as

$$\frac{p - p_D}{\rho_0} = -\langle b\rangle_{D-z}(D - z) - \left.\frac{w^2}{2}\right|_z. \tag{C3}$$

Equation (C3) illustrates that pressure p comprises a hydrostatic component, $\langle b\rangle_{D-z}(D - z)$, and a non-hydrostatic component, $w^2/2$.

Appendix D. Cross-shore momentum balance

We start with regime I and focus on the cross-shore momentum balance during regime I:

$$\frac{\partial u}{\partial t} + \boldsymbol{v} \cdot \boldsymbol{\nabla} u = -\frac{1}{\rho_0}\frac{\partial p}{\partial x} + \nu \nabla^2 u. \tag{D1}$$

One approach consists of considering a three-way linear momentum balance between the inertial, the viscous and the cross-shore pressure gradient terms to derive asymptotic solutions for the cross-shore velocity at small slopes and low Ra (Farrow & Patterson 1993). Alternatively, we can follow the approach adopted by Finnigan & Ivey (1999) and integrate the role of advection, $\boldsymbol{v} \cdot \boldsymbol{\nabla} u$, on the formation of a horizontal overturning due to an increase in time of the cross-shore pressure gradient. Neglecting the viscous term in (E1*a–c*), and considering that once the large-scale overturning circulation starts the flow becomes largely horizontal, (E1*a–c*) reduces to the following three-way momentum balance:

$$\frac{\partial u}{\partial t} + \frac{\partial}{\partial x}\left(\frac{u^2}{2}\right) \approx -\frac{\partial}{\partial x}\left(\frac{p}{\rho_0}\right). \tag{D2}$$

The cross-shore pressure gradient at $z = D - d$, the depth of zone (P), increases in time due to differential cooling. From (C3) and (4.8*a*,*b*), we can estimate $\partial p/\partial x$ directly from the cross-shore temperature gradient:

$$\frac{1}{\rho_0}\frac{\partial p}{\partial x} = dg\alpha\frac{\partial}{\partial x}\langle T\rangle_{D-z}. \tag{D3}$$

A constant sloping bottom induces a uniform pressure gradient across zone (S). Thus, recalling that $B_0 = -g\alpha I_0$, the time-dependent, cross-shore pressure gradient between zones (P) and (I) can be

https://doi.org/10.1017/flo.2024.31 Published online by Cambridge University Press

estimated from (B3) and (B6) as

$$\frac{1}{\rho_0}\frac{\partial p}{\partial x}\bigg|_{z=D-d} \approx \frac{dg\alpha}{\ell_s}(\langle T\rangle_{(I)} - \langle T\rangle_{(P)}) = -\frac{B_0}{\ell_s}\left(1-\frac{d}{h_m}\right)t. \tag{D4}$$

In general, the horizontal temperature difference $\langle T\rangle_{(I)} - \langle T\rangle_{(P)}$ is substantially smaller than the temperature difference between the top and bottom layers in the stratified interior region (I), ΔT.

Appendix E. Non-dimensional numbers and Boussinesq equations

In the previous subsections we have described the physics and the dynamic balances needed to derive the time scales setting the pace at which a TS develops due to a destabilising surface cooling in sloping water bodies with conditions similar to those sketched in figure 3(*c*,*d*). We now turn the focus to the non-dimensional numbers and governing equations needed to model the thermohydrodynamics of TS and test further the introduced time scales via numerical and field experiments.

Considering the parameters introduced in § 4.1 $\{d, h'_m, \ell_p, \ell_s, g', w_c, \nu, \kappa\}$, and the Buckingham Π theorem, we derive six non-dimensional numbers including three parameters characterising the water body geometry,

$$\bar{s} = \frac{h'_m}{\ell_s}, \quad A^{(v)} = \frac{d}{h_m}, \quad A^{(h)} = \frac{\ell_p}{\ell_s}, \tag{E1a–c}$$

and three parameters characterising the flow dynamics,

$$Pr = \frac{\nu}{\kappa}, \quad Ri_c = \frac{g'h'_m}{w_c^2}, \quad Ra = \frac{w_c h'_m}{\kappa}. \tag{E2a–c}$$

Note that the parameters $h'_m = h_m - d$ and ℓ_s encapsulate the intrinsic vertical and horizontal length scales associated with the characteristic slope $\bar{s}$ between the plateau region and the interior region. The second parameter in (E1*a*–*c*) describes the ratio between the shallow depth and the mixing layer depth. We expect that as $A^{(v)} \to 0$, the difference between the cooling rate of the shallow and the cooling rate of the interior region becomes larger, thus speeding up the TS formation. The third parameter, $A^{(h)}$, describes the ratio between the horizontal length scales of zones (P) and (S). Thus, fixing ℓ_s, one expects that smaller values of $A^{(h)}$ are associated with shorter time windows between the formation and the stabilisation of TS.

The first parameter in (E1*a*–*c*) is the Prandtl number, the ratio of viscous diffusivity to thermal diffusivity, Here set to be $Pr = 7$ to model temperate thermally stratified freshwater bodies. The second parameter, the convective Richardson number Ri_c, compares the ratio of stabilising effects of stratification to the destabilising effects of convective stirring. The third parameter in (E1*a*–*c*), the Rayleigh number Ra – defined as the ratio of advective to diffusive heat transport – establishes the intensity of the destabilising buoyancy force propelling to convection. Note that this non-dimensional parameter can also be interpreted as a Péclet number.

To evaluate the influence of non-dimensional numbers in the equations of motion, we normalise the dimensional variables by considering the convective characteristic scales as follows:

$$x \sim \ell_s, \quad z \sim h'_m, \quad t \sim h'_m/w_c, \quad \boldsymbol{v} \sim w_c, \quad p \sim \rho_0 w_c^2 \quad \text{and} \quad \rho \sim \Delta\rho. \tag{E3a–f}$$

We utilise the same characteristic scales to non-dimensionalise the spatial and temporal derivatives, i.e.

$$\tilde{\boldsymbol{\nabla}}_{\bar{s}} = \bar{s}\left(\frac{\partial}{\partial\tilde{x}}\hat{\mathbf{i}} + \frac{\partial}{\partial\tilde{y}}\hat{\mathbf{j}}\right) + \frac{\partial}{\partial\tilde{z}}\hat{\mathbf{k}} \quad \text{and} \quad \tilde{\nabla}^2_{\bar{s}} \equiv \tilde{\boldsymbol{\nabla}}_{\bar{s}} \cdot \tilde{\boldsymbol{\nabla}}_{\bar{s}} = \bar{s}^2\left(\frac{\partial^2}{\partial\tilde{x}^2} + \frac{\partial^2}{\partial\tilde{y}^2}\right) + \frac{\partial^2}{\partial\tilde{z}^2}, \tag{E4a,b}$$

https://doi.org/10.1017/flo.2024.31 Published online by Cambridge University Press

the non-dimensional governing equations are given by

$$\frac{\partial \tilde{T}}{\partial \tilde{t}} + \tilde{\boldsymbol{v}} \cdot \tilde{\boldsymbol{\nabla}}_{\bar{s}} = \frac{1}{Ra} \tilde{\nabla}^2_{\bar{s}} \tilde{T}, \tag{E5a}$$

$$\frac{\partial \tilde{\boldsymbol{v}}}{\partial \tilde{t}} + \tilde{\boldsymbol{v}} \cdot \tilde{\boldsymbol{\nabla}}_{\bar{s}} = -\tilde{\boldsymbol{\nabla}}_{\bar{s}} \tilde{p} - Ri_c \tilde{\rho} \hat{\mathbf{k}} + \frac{Pr}{Ra} \tilde{\nabla}^2_{\bar{s}} \tilde{\boldsymbol{v}}, \tag{E5b}$$

$$\tilde{\boldsymbol{\nabla}}_{\bar{s}} \cdot \tilde{\boldsymbol{v}} = 0, \tag{E5c}$$

where $(\tilde{\cdot})$ denotes non-dimensional variables. The non-dimensional numbers $\bar{s}$, Pr, Ri_c and Ra describe the relative importance of the various terms in the governing equations (E5). The latter provides insights into their role in the momentum and energy balances. Firstly, the slope, $\bar{s}$, weights the cross-shore component of the advective acceleration and pressure gradient. Secondly, the convective Richardson number, Ri_c, weights the buoyancy, or gravity force, in the vertical momentum balance (z axis). Thirdly, the diffusion of momentum and heat is inversely proportional to the Rayleigh number, $(PrRa^{-1})\tilde{\nabla}^2_{\bar{s}}\tilde{\boldsymbol{v}}$ and $(Ra^{-1})\tilde{\nabla}^2_{\bar{s}}\tilde{T}$, respectively.

In practical scenarios, such as the study of TS in inland waters, Ra is significantly greater than the critical value for Rayleigh–Bénard convection. High Ra ($Ra \gtrsim 10^4$ considering the definition in (E1*a–c*)) guarantees the development of a vigorous convective regime, wherein convection exerts a dominant influence on transport, overshadowing the contributions of momentum and heat diffusion in the dynamic and energy balances.

Acknowledgements. The authors thank J. Wüest and K. Winters for previous discussions on this topic. The authors also thank M. Wells and a second reviewer for their detailed comments. Finally, the authors thank the Associate Editor Greg Ivey.

Funding statement. D.B. acknowledges support from the Swiss National Science Foundation, Grant 200021-175919, buoyancy-driven nearshore transport in lakes, HYPOlimnetic THErmal SYphonS (HYPOTHESYS).

Declaration of interests. The authors declare no conflict of interest.

Author contributions. Conceptualisation: all. Formal analysis: CRC, HU, TD. Results interpretation and discussion: all. Writing: all. Visualisation: all. Funding acquisition: DB.

Ethical standards. The research meets all ethical guidelines, including adherence to the legal requirements of the study country.

References

Adams, E. & Wells, S.A. 1984 Field measurements on side arms of Lake Anna, VA. *J. Hydraul. Engng* **110** (6), 773–793.

Amber, I. & O'Donovan, T. 2018 Natural convection induced by the absorption of solar radiation: a review. *Renew. Sust. Energy Rev.* **82**, 3526–3545.

Ambrosetti, W., Barbanti, L. & Carrara, E.A. 2010 Mechanisms of hypolimnion erosion in a deep lake (Lago Maggiore, N. Italy). *J. Limnol.* **69** (1), 3.

Baines, W.D. 1975 Entrainment by a plume or jet at a density interface. *J. Fluid Mech.* **68** (2), 309–320.

Bednarz, T.P., Lei, C. & Patterson, J.C. 2008*a* An experimental study of unsteady natural convection in a reservoir model cooled from the water surface. *Expl Therm. Fluid Sci.* **32** (3), 844–856.

Bednarz, T.P., Lei, C. & Patterson, J.C. 2008*b* An experimental study of unsteady natural convection in a reservoir model cooled from the water surface. *Expl Therm. Fluid Sci.* **32** (3), 844–856.

Bednarz, T.P., Lei, C. & Patterson, J.C. 2009*a* A numerical study of unsteady natural convection induced by iso-flux surface cooling in a reservoir model. *Intl J. Heat Mass Transfer* **52** (1–2), 56–66.

Bednarz, T.P., Lei, C. & Patterson, J.C. 2009*b* Unsteady natural convection induced by diurnal temperature changes in a reservoir with slowly varying bottom topography. *Intl J. Therm. Sci.* **48** (10), 1932–1942.

Biemond, B., Amadori, M., Toffolon, M., Piccolroaz, S., Haren, H.V., Dijkstra, H.A. 2021 Deep-mixing and deep-cooling events in Lake Garda: simulation and mechanisms. *J. Limnol.* **80** (2).

Biton, E., Silverman, J. & Gildor, H. 2008 Observations and modeling of a pulsating density current. *Geophys. Res. Lett.* **35**, L14603.

Bouffard, D. & Wüest, A. 2019 Convection in lakes. *Annu. Rev. Fluid Mech.* **51**, 189–215.

Bouffard, D., *et al.* 2019 Under-ice convection dynamics in a boreal lake. *Inland Waters* **9**, 142–161.

Boyce, F., Donelan, M.A., Hamblin, P., Murthy, C. & Simons, T.J. 1989 Thermal structure and circulation in the great lakes. *Atmos. Ocean* **27** (4), 607–642.

https://doi.org/10.1017/flo.2024.31 Published online by Cambridge University Press

Brooks, I. & Lick, W. 1972 Lake currents associated with the thermal bar. *J. Geophys. Res*. **77** (30), 6000–6013.

Cannaby, H., White, M. & Bowyer, P. 2007 Dynamical response to differential rates of temperature change over sloping topography: Lough Corrib, Ireland. *J. Geophys. Res*. **112**, C09009.

Carmack, E.C., Gray, C.B.J., Pharo, C.H. & Daley, R.J. 1979 Importance of lake-river interaction on seasonal patterns in the general circulation of Kamloops Lake, British Columbia. *Limnol. Oceanogr*. **24** (4), 634–644.

de Carvalho Bueno, R., Bleninger, T. & Lorke, A. 2021 Internal wave analyzer for thermally stratified lakes. *Environ. Model. Softw*. **136**, 104950.

Cenedese, C. & Adduce, C. 2010 A new parameterization for entrainment in overflows. *J. Phys. Oceanogr*. **40** (8), 1835–1850.

Chen, C.-T.A. & Millero, F.J. 1986 Thermodynamic properties for natural waters covering only the limnological range. *Limnol. Oceanogr*. **31** (3), 657–662.

Christodoulou, G.C. 1986 Interfacial mixing in stratified flows. *J. Hydraul. Res*. **24** (2), 77–92.

Chubarenko, I.P., Esiukova, E., Stepanova, N., Chubarenko, B. & Baudler, H. 2013 Down-slope cascading modulated by day/night variations of solar heating. *J. Limnol*. **72** (2), e19.

Coenen, W., Sánchez, A., Félez, R., Davis, K. & Pawlak, G. 2021 Residual streaming flows in buoyancy-driven cross-shore exchange. *J. Fluid Mech*. **920**, A1.

Cortés, A., Fleenor, W., Wells, M., De Vicente, I. & Rueda, F. 2014 Pathways of river water to the surface layers of stratified reservoirs. *Limnol. Oceanogr*. **59** (1), 233–250.

Cortés, A. & MacIntyre, S. 2020 Mixing processes in small arctic lakes during spring. *Limnol. Oceanogr*. **65**, 260–288.

Cotel, A.J. & Kudo, Y. 2008 Impingement of buoyancy-driven flows at a stratified interface. *Exp. Fluids* **45** (1), 131–139.

D'Asaro, E.A., Winters, K.B. & Lien, R.-C. 2002 Lagrangian analysis of a convective mixed layer. *J. Geophys. Res*. **107** (C5), 571–622.

Davis, S.R., Farrar, J.T., Weller, R.A., Jiang, H. & Pratt, L.J. 2019 The land-sea breeze of the red sea: observations, simulations, and relationships to regional moisture transport. *J. Geophys. Res*. **124** (24), 13803–13825.

Deardorff, J.W. 1970 Convective velocity and temperature scales for the unstable planetary boundary layer and for Rayleigh convection. *J. Atmos. Sci*. **27** (8), 1211–1213.

Deardorff, J.W., Willis, G.E. & Lilly, D.K. 1969 Laboratory investigation of non-steady penetrative convection. *J. Fluid Mech*. **35** (1), 7–31.

Deardorff, J.W., Willis, G.E. & Stockton, B.H. 1980 Laboratory studies of the entrainment zone of a convectively mixed layer. *J. Fluid Mech*. **100** (1), 41–64.

Doda, T. 2022 Density currents driven by differential cooling in lakes: occurrence, dynamics and implications for littoral-pelagic exchange. PhD thesis, EPFL, Ecole Polytechnique Fédérale de Lausanne.

Doda, T., Ramón, C.L., Ulloa, H.N., Brennwald, M.S., Kipfer, R., Perga, M.-E., Wüest, A., Schubert, C.J. & Bouffard, D. 2024 Lake surface cooling drives littoral-pelagic exchange of dissolved gases. *Sci. Adv*. **10** (4), eadi0617.

Doda, T., Ramón, C.L., Ulloa, H.N., Wüest, A. & Bouffard, D. 2022 Seasonality of density currents induced by differential cooling. *Hydrol. Earth Syst. Sci*. **26** (2), 331–353.

Doda, T., Ulloa, H.N., Ramón, C.L., Wüest, A. & Bouffard, D. 2023 Penetrative convection modifies the dynamics of downslope gravity currents. *Geophys. Res. Lett*. **50** (2), e2022GL100633.

Eccles, D.H. 1974 An outline of the physical limnology of Lake Malawi (Lake Nyasa). *Limnol. Oceanogr*. **19** (5), 730–742.

El Gdachi, S., Tulet, P., Réchou, A., Burnet, F., Mouchel-Vallon, C., Jambert, C. & Leriche, M. 2024 Thermodynamic processes driving thermal circulations on slopes: modeling anabatic and katabatic flows on reunion island. *J. Geophys. Res*. **129** (17), e2023JD040431.

Ellison, T.H. & Turner, J.S. 1959 Turbulent entrainment in stratified flows. *J. Fluid Mech*. **6** (3), 423–448.

Fang, X. & Stefan, H.G. 1996 Dynamics of heat exchange between sediment and water in a lake. *Water Resour. Res*. **32** (6), 1719–1727.

Farmer, D.M. 1975 Penetrative convection in the absence of mean shear. *Q. J. R. Meteorol. Soc*. **101** (430), 869–891.

Farmer, D.M. & Armi, L. 1986 Maximal two-layer exchange over a sill and through the combination of a sill and contraction with barotropic flow. *J. Fluid Mech*. **164**, 53–76.

Farrow, D. & Patterson, J. 1993 On the response of a reservoir sidearm to diurnal heating and cooling. *J. Fluid Mech*. **246**, 143–161.

Farrow, D.E. 1995*a* An asymptotic model for the hydrodynamics of the thermal bar. *J. Fluid Mech*. **289**, 129–140.

Farrow, D.E. 1995*b* A numerical model of the hydrodynamics of the thermal bar. *J. Fluid Mech*. **303**, 279–295.

Farrow, D.E. 2004 Periodically forced natural convection over slowly varying topography. *J. Fluid Mech*. **508**, 1–21.

Farrow, D.E. 2013*a* A model for the evolution of the thermal bar system. *Eur. J. Appl. Maths* **24** (2), 161–177.

Farrow, D.E. 2013*b* Periodically driven circulation near the shore of a lake. *Environ. Fluid Mech*. **13**, 243–255.

Farrow, D.E. 2016 A numerical model of periodically forced circulation near the shore of a lake. *Environ. Fluid Mech*. **16**, 983–995.

Farrow, D.E. & McDonald, N.R. 2002 Coriolis effects and the thermal bar. *J. Geophys. Res*. **107** (C5), 1–1.

Fer, I., Lemmin, U. & Thorpe, S. 2002*a* Winter cascading of cold water in Lake Geneva. *J. Geophys. Res*. **107** (C6), 13–1.

Fer, I., Lemmin, U. & Thorpe, S.A. 2001 Cascading of water down the sloping sides of a deep lake in winter. *Geophys. Res. Lett*. **28** (10), 2093–2096.

https://doi.org/10.1017/flo.2024.31 Published online by Cambridge University Press

Fer, I., Lemmin, U. & Thorpe, S.A. 2002*b* Contribution of entrainment and vertical plumes to the winter cascading of cold shelf waters in a deep lake. *Limnol. Oceanogr.* **47** (2), 576–580.

Finnigan, T.D. & Ivey, G.N. 1999 Submaximal exchange between a convectively forced basin and a large reservoir. *J. Fluid Mech.* **378**, 357–378.

Finnigan, T.D. & Ivey, G.N. 2000 Convectively driven exchange flow in a stratified sill-enclosed basin. *J. Fluid Mech.* **418**, 313–338.

Forel, F. 1880 La congélation des lacs suisses et savoyards pendant l'hiver 1879–1880.11 – Lac Léman. *L'Écho des Alpes* **3**, 149–161.

Forrest, A.L., Laval, B.E., Pieters, R. & Lim, D.S. 2008 Convectively driven transport in temperate lakes. *Limnol. Oceanogr.* **53** (5part2), 2321–2332.

Forrest, A.L., Laval, B.E., Pieters, R. & Lim, D.S.S. 2013 A cyclonic gyre in an ice-covered lake. *Limnol. Oceanogr.* **58**, 363–375.

Gayen, B., Griffiths, R.W., Hughes, G.O. & Saenz, J.A. 2013 Energetics of horizontal convection. *J. Fluid Mech.* **716**, R10.

Griffiths, R.W., Hughes, G.O. & Gayen, B. 2013 Horizontal convection dynamics: insights from transient adjustment. *J. Fluid Mech.* **726**, 559–595.

Grimes, D., Feddersen, F. & Kumar, N. 2020 Tracer exchange across the stratified inner-shelf driven by transient rip-currents and diurnal surface heat fluxes. *Geophys. Res. Lett.* **47** (10), e2019GL086501.

Helfrich, K.R. 1995 Time-dependent two-layer hydraulic exchange flows. *J. Phys. Oceanogr.* **25** (3), 359–373.

Hetzel, Y., Pattiaratchi, C., Lowe, R. & Hofmeister, R. 2015 Wind and tidal mixing controls on stratification and dense water outflows in a large hypersaline bay. *J. Geophys. Res.* **120** (9), 6034–6056.

Hidalgo, J., Masson, V. & Gimeno, L. 2010 Scaling the daytime urban heat island and urban-breeze circulation. *J. Appl. Meteorol. Climatol.* **49** (5), 889–901.

Hogg, A.M., Ivey, G.N. & Winters, K.B. 2001 Hydraulics and mixing in controlled exchange flows. *J. Geophys. Res.* **106** (C1), 959–972.

Hogg, C.A., Marti, C.L., Huppert, H.E. & Imberger, J. 2013 Mixing of an interflow into the ambient water of Lake Iseo. *Limnol. Oceanogr.* **58** (2), 579–592.

Holland, P.R. & Kay, A. 2003 A review of the physics and ecological implications of the thermal bar circulation. *Limnologica* **33** (3), 153–162.

Hondzo, M. & Stefan, H.G. 1993 Lake water temperature simulation model. *J. Hydraul. Engng* **119** (11), 1251–1273.

Horsch, G., Stefan, H. & Gavali, S. 1994 Numerical simulation of cooling-induced convective currents on a littoral slope. *Intl J. Numer. Meth. Fluids* **19** (2), 105–134.

Horsch, G.M. & Stefan, H.G. 1988 Convective circulation in littoral water due to surface cooling. *Limnol. Oceanogr.* **33** (5), 1068–1083.

Huang, J.C.K. 1972 The thermal bar. *Geophys. Fluid Dyn.* **3** (1), 1–25.

Hughes, G.O., Gayen, B. & Griffiths, R.W. 2013 Available potential energy in Rayleigh–Bénard convection. *J. Fluid Mech.* **729**, R3.

Hughes, G.O. & Griffiths, R.W. 2008 Horizontal convection. *Annu. Rev. Fluid Mech.* **40**, 185–208.

Imberger, J. 1985 The diurnal mixed layer. *Limnol. Oceanogr.* **30** (4), 737–770.

Imberger, J. & Patterson, J.C. 1989 Physical limnology. *Adv. Appl. Mech.* **27**, 303–475.

Ivanov, V., Shapiro, G., Huthnance, J., Aleynik, D. & Golovin, P. 2004 Cascades of dense water around the world ocean. *Prog. Oceanogr.* **60** (1), 47–98.

Ivey, G. 2004 Stratification and mixing in sea straits. *Deep-Sea Res.* II **51** (4–5), 441–453.

Jabbari, A., Ackerman, J.D., Boegman, L. & Zhao, Y. 2019 Episodic hypoxia in the western basin of Lake Erie. *Limnol. Oceanogr.* **64** (5), 2220–2236.

James, W.F. & Barko, J.W. 1991*a* Estimation of phosphorus exchange between littoral and pelagic zones during nighttime convective circulation. *Limnol. Oceanogr.* **36** (1), 179–187.

James, W.F. & Barko, J.W. 1991*b* Littoral-pelagic phosphorus dynamics during nighttime convective circulation. *Limnol. Oceanogr.* **36** (5), 949–960.

James, W.F., Barko, J.W. & Eakin, H.L. 1994 Convective water exchanges during differential cooling and heating: implications for dissolved constituent transport. *Hydrobiologia* **294**, 167–176.

Kenney, B.C. 1996 Physical limnological processes under ice. In *The First International Lake Ladoga Symposium: Proceedings of the First International Lake Ladoga Symposium: Ecological Problems of Lake Ladoga* (ed. H. Simola, M. Viljanen, T. Slepukhina & R. Murthy), pp. 85–90. Springer.

Kirillin, G., Forrest, A., Graves, K., Fischer, A., Engelhardt, C. & Laval, B. 2015 Axisymmetric circulation driven by marginal heating in ice-covered lakes. *Geophys. Res. Lett.* **42** (8), 2893–2900.

Kirillin, G., *et al.* 2012 Physics of seasonally ice-covered lakes: a review. *Aquat. Sci.* **74**, 659–682.

Kratz, T.K., MacIntyre, S. & Webster, K.E. 2005 Causes and consequences of spatial heterogeneity in lakes. In *Ecosystem Function in Heterogeneous Landscapes* (ed. G.M. Lovett, M.G. Turner, C.G. Jones, & K.C. Weathers), pp. 329–347. Springer.

Lei, C. & Patterson, J.C. 2002 Unsteady natural convection in a triangular enclosure induced by absorption of radiation. *J. Fluid Mech.* **460**, 181–209.

https://doi.org/10.1017/flo.2024.31 Published online by Cambridge University Press

Lei, C. & Patterson, J.C. 2003 A direct stability analysis of a radiation-induced natural convection boundary layer in a shallow wedge. *J. Fluid Mech.* **480**, 161–184.

Lei, C. & Patterson, J.C. 2005 Unsteady natural convection in a triangular enclosure induced by surface cooling. *Intl J. Heat Fluid Flow* **26** (2), 307–321.

Lemmin, U. 2020 Insights into the dynamics of the deep hypolimnion of Lake Geneva as revealed by long-term temperature, oxygen, and current measurements. *Limnol. Oceanogr.* **65** (9), 2092–2107.

Lennon, G., *et al.* 1987 Gravity currents and the release of salt from an inverse estuary. *Nature* **327** (6124), 695–697.

Lentz, S.J. & Fewings, M.R. 2012 The wind-and wave-driven inner-shelf circulation. *Annu. Rev. Mar. Sci.* **4**, 317–343.

Leppäranta, M. 2015 *Freezing of Lakes and the Evolution of their Ice Cover*. Springer.

Likens, G.E. & Ragotzkie, R.A. 1966 Rotary circulation of water in an ice-covered lake. In *Proceedings of the International Society of Limnology 1922–2010*, vol. 16, pp. 126–133. Taylor & Francis.

Lin, Y.-T. 2015 Wind effect on diurnal thermally driven flow in vegetated nearshore of a lake. *Environ. Fluid Mech.* **15**, 161–178.

Lin, Y.-T. & Wu, C.H. 2014 The role of rooted emergent vegetation on periodically thermal-driven flow over a sloping bottom. *Environ. Fluid Mech.* **14**, 1303–1334.

Linden, P.F. & Simpson, J.E. 1986 Gravity-driven flows in a turbulent fluid. *J. Fluid Mech.* **172**, 481–497.

Lövstedt, C.B. & Bengtsson, L. 2008 Density-driven current between reed belts and open water in a shallow lake. *Water Resour. Res.* **44**, W10413.

MacIntyre, S., Cortés, A. & Sadro, S. 2018 Sediment respiration drives circulation and production of CO_2 in ice-covered Alaska Arctic lakes. *Limnol. Oceanogr. Lett.* **3** (3), 302–310.

MacIntyre, S. & Melack, J.M. 1995 Vertical and horizontal transport in lakes: linking littoral, benthic, and pelagic habitats. *J. N. Am. Benthol. Soc.* **14** (4), 599–615.

Mahjabin, T., Pattiaratchi, C. & Hetzel, Y. 2019 Wind effects on dense shelf water cascades in south-west Australia. *Cont. Shelf Res.* **189**, 103975.

Malm, J. 1995 Spring circulation associated with the thermal bar in large temperate lakes. *Hydrol. Res.* **26** (4–5), 331–358.

Malm, J., Grahn, L., Mironov, D. & Terzhevik, A. 1993 Field investigation of the thermal bar in Lake Ladoga, Spring 1991. *Hydrol. Res.* **24** (5), 339–358.

Mao, Y. 2019 Nearshore natural convection induced by a periodic thermal forcing at the water surface. *Phys. Fluids* **31** (8), 086604.

Mao, Y., Lei, C. & Patterson, J.C. 2009 Unsteady natural convection in a triangular enclosure induced by absorption of radiation–a revisit by improved scaling analysis. *J. Fluid Mech.* **622**, 75–102.

Mao, Y., Lei, C. & Patterson, J.C. 2010 Unsteady near-shore natural convection induced by surface cooling. *J. Fluid Mech.* **642**, 213–233.

Mao, Y., Lei, C. & Patterson, J.C. 2012 Unsteady nearshore natural convection induced by constant isothermal surface heating. *J. Fluid Mech.* **707**, 342–368.

Mao, Y., Lei, C. & Patterson, J.C. 2019 Natural convection in a reservoir induced by sinusoidally varying temperature at the water surface. *Intl J. Heat Mass Transfer* **134**, 610–627.

Miller, S., Keim, B., Talbot, R. & Mao, H. 2003 Sea breeze: structure, forecasting, and impacts. *Rev. Geophys.* **41**, 1011.

Mironov, D., Terzhevik, A., Kirillin, G., Jonas, T., Malm, J. & Farmer, D. 2002 Radiatively driven convection in ice-covered lakes: observations, scaling, and a mixed layer model. *J. Geophys. Res.* **107** (C4), 7–1.

Molina, L., Pawlak, G., Wells, J., Monismith, S. & Merrifield, M. 2014 Diurnal cross-shore thermal exchange on a tropical forereef. *J. Geophys. Res.* **119** (9), 6101–6120.

Monismith, S.G., Genin, A., Reidenbach, M.A., Yahel, G. & Koseff, J.R. 2006 Thermally driven exchanges between a coral reef and the adjoining ocean. *J. Phys. Oceanogr.* **36** (7), 1332–1347.

Monismith, S.G., Imberger, J. & Morison, M.L. 1990 Convective motions in the sidearm of a small reservoir. *Limnol. Oceanogr.* **35** (8), 1676–1702.

Monsen, N.E., Cloern, J.E., Lucas, L.V. & Monismith, S.G. 2002 A comment on the use of flushing time, residence time, and age as transport time scales. *Limnol. Oceanogr.* **47** (5), 1545–1553.

Montlaur, A., Arias, S. & Rojas, J.I. 2024 Thermally driven winds on mars: a review and a slope effect numerical study. *J. Geophys. Res.* **129** (4), e2023JE007987.

Moore, M.J. & Long, R.R. 1971 An experimental investigation of turbulent stratified shearing flow. *J. Fluid Mech.* **49** (4), 635–655.

Mortimer, C. 1953 The resonant response of stratified lakes to wind. *Schweiz. Z. Hydrol.* **15**, 94–151.

Nepf, H.M. 2012 Flow and transport in regions with aquatic vegetation. *Annu. Rev. Fluid Mech.* **44**, 123–142.

Noh, Y., Fernando, H.J.S. & Ching, C.Y. 1992 Flows induced by the impingement of a two-dimensional thermal on a density interface. *J. Phys. Oceanogr.* **22** (10), 1207–1220.

Noto, D., Ulloa, H.N., Yanagisawa, T. & Tasaka, Y. 2023 Stratified horizontal convection. *J. Fluid Mech.* **970**, A21.

Pálmarsson, S.Ó. & Schladow, S.G. 2008 Exchange flow in a shallow lake embayment. *Ecol. Appl.* **18** (8sp8), A89–A106.

Papaioannou, V. & Prinos, P. 2023 Natural convection due to surface cooling in sloping water bodies with vegetation. *J. Hydraul. Res.* **61** (3), 382–395.

Parker, D.J., Burton, R.R., Diongue-Niang, A., Ellis, R.J., Felton, M., Taylor, C.M., Thorncroft, C.D., Bessemoulin, P. & Tompkins, A.M. 2005 The diurnal cycle of the West African monsoon circulation. *Q. J. R. Meteorolo. Soc.* **131** (611), 2839–2860.

https://doi.org/10.1017/flo.2024.31 Published online by Cambridge University Press

Peeters, F., Finger, D., Hofer, M., Brennwald, M., Livingstone, D.M. & Kipfer, R. 2003 Deep-water renewal in Lake Issyk-Kul driven by differential cooling. *Limnol. Oceanogr*. **48** (4), 1419–1431.

Peng, N., Lemmin, U., Mettra, F., Reiss, R. & Barry, D. 2024 Deepwater renewal in a large, deep lake (Lake Geneva): identifying and quantifying winter cooling processes using heat budget decomposition. *Water Resour. Res*. **60** (4), e2023WR034936.

Perga, M.-E., *et al.* 2023 Near-bed stratification controls bottom hypoxia in ice-covered alpine lakes. *Limnol. Oceanogr*. **68** (6), 1232–1246.

Phillips, O. 1966 On turbulent convection currents and the circulation of the Red Sea. *Deep-Sea Res*. **13** (6), 1149–1160.

Prinos, P. & Papaioannou, V. 2024*a* Diurnal heating and cooling of a sloping water body with vegetated shallow regions. *Environ. Fluid Mech*. **24**, 57–74.

Prinos, P. & Papaioannou, V. 2024*b* Vegetation effects on radiation-induced natural convection in sloping water bodies. *Environ. Fluid Mech*. **24**, 119–138.

Ramón, C., Priet-Mahéo, M., Rueda, F. & Andradóttir, H. 2020 Inflow dynamics in weakly stratified lakes subject to large isopycnal displacements. *Water Resour. Res*. **56** (8), e2019WR026578.

Ramón, C.L., Ulloa, H.N., Doda, T. & Bouffard, D. 2022 Flushing the lake littoral region: the interaction of differential cooling and mild winds. *Water Resour. Res*. **58** (3), e2021WR030943.

Ramón, C.L., Ulloa, H.N., Doda, T., Winters, K.B. & Bouffard, D. 2021 Bathymetry and latitude modify lake warming under ice. *Hydrol. Earth Syst. Sci*. **25** (4), 1813–1825.

Razlutskij, V.I., Buseva, Z.F., Feniova, Y.I. & Semenchenko, V.P. 2021 Convective circulation influences horizontal movement by planktonic crustaceans in the littoral zone of a mesotrophic lake. *Freshw. Biol*. **66** (4), 716–729.

Read, J.S., Hamilton, D.P., Jones, I.D., Muraoka, K., Winslow, L.A., Kroiss, R., Wu, C.H. & Gaiser, E. 2011 Derivation of lake mixing and stratification indices from high-resolution lake buoy data. *Environ. Model. Softw*. **26** (11), 1325–1336.

Reiss, R.S., Lemmin, U. & Barry, D. 2022 Wind-induced hypolimnetic upwelling between the multi-depth basins of lake Geneva during winter: an overlooked deepwater renewal mechanism? *J. Geophys. Res*. **127** (6), e2021JC018023.

Roget, E., Colomer, J., Casamitjana, X. & Llebot, J. 1993 Bottom currents induced by baroclinic forcing in Lake Banyoles (Spain). *Aquat. Sci*. **55**, 206–227.

Rogowski, P., Merrifield, S., Ding, L., Terrill, E. & Gesiriech, G. 2019 Robotic mapping of mixing and dispersion of augmented surface water in a drought frequent reservoir. *Limnol. Oceanogr*. **17** (9), 475–489.

Rossby, H. 1965 On thermal convection driven by non-uniform heating from below: an experimental study. In *Deep-Sea Res. Oceanogr. Abstr.* **12** (1), 9–16.

Rueda, F., Moreno-Ostos, E. & Cruz-Pizarro, L. 2007 Spatial and temporal scales of transport during the cooling phase of the ice-free period in a small high-mountain lake. *Aquat. Sci*. **69**, 115–128.

Safaie, A., Pawlak, G. & Davis, K.A. 2022 Diurnal thermally driven cross-shore exchange in steady alongshore currents. *J. Geophys. Res*. **127** (4), e2021JC017912.

Salonen, K., Pulkkanen, M., Salmi, P. & Griffiths, R.W. 2014 Mixing processes in small arctic lakes during spring. *Limnol. Oceanogr*. **59**, 2121–2132.

Schmid, M. & Read, J. 2022 Heat budget of lakes. In *Encyclopedia of Inland Waters*, 2nd edn (ed. T. Mehner & K. Tockner), pp. 467–473. Elsevier.

Sha, W., Kawamura, T. & Ueda, H. 1991 A numerical study on sea/land breezes as a gravity current: Kelvin–Helmholtz billows and inland penetration of the sea-breeze front. *J. Atmos. Sci*. **48** (14), 1649–1665.

Shapiro, G.I. 2003 Dense water cascading off the continental shelf. *J. Geophys. Res*. **108** (C12), 3390.

Simpson, J.E. 1986 Mixing at the front of a gravity current. *Acta Mechanica* **63** (1–4), 245–253.

Simpson, J.E., Mansfield, D.A. & Milford, J.R. 1977 Inland penetration of sea-breeze fronts. *Q. J. R. Meteorol. Soc*. **103** (435), 47–76.

Soloviev, A. & Lukas, R. 2014 *The Near-Surface Layer of the Ocean: Structure, Dynamics, and Applications*, 2nd edn, Atmospheric and Oceanographic Sciences Library, vol. 48. Springer.

Stefan, H.G., Horsch, G. & Barko, J.W. 1989 A model for the estimation of convective exchange in the littoral region of a shallow lake during cooling. *Hydrobiologia* **174**, 225–234.

Stefanovic, D.L. & Stefan, H.G. 2002 Two-dimensional temperature and dissolved oxygen dynamics in the littoral region of an ice-covered lake. *Cold. Reg. Sci. Technol*. **34**, 159–178.

Sturman, J. & Ivey, G. 1998 Unsteady convective exchange flows in cavities. *J. Fluid Mech*. **368**, 127–153.

Sturman, J., Ivey, G. & Taylor, J. 1996 Convection in a long box driven by heating and cooling on the horizontal boundaries. *J. Fluid Mech*. **310**, 61–87.

Sturman, J.J., Oldham, C.E. & Ivey, G.N. 1999 Steady convective exchange flows down slopes. *Aquat. Sci*. **61**, 260–278.

Sullivan, P.P., Moeng, C. -H., Stevens, B., Lenschow, D.H. & Mayor, S.D. 1998 Structure of the entrainment zone capping the convective atmospheric boundary layer. *J. Atmos. Sci*. **55** (19), 3042–3064.

Talling, J. 1963 Origin of stratification in an african rift lake. *Limnol. Oceanogr*. **8** (1), 68–78.

Terzhevik, A. 2012 *Thermal Bar*, pp. 795–797.Springer.

Thorpe, S. 1999 Observations of the thermal structure of a lake using a submarine. *Limnol. Oceanogr*. **44** (6), 1575–1582.

Tsydenov, B.O. 2018 Numerical modeling of the autumnal thermal bar. *J. Mar. Syst*. **179**, 1–9.

Tsydenov, B.O. 2019 A numerical study of the thermal bar in shallow water during the autumn cooling. *J. Great Lakes Res*. **45** (4), 715–725.

https://doi.org/10.1017/flo.2024.31 Published online by Cambridge University Press

Ulloa, H.N., Davis, K.A., Monismith, S.G. & Pawlak, G. 2018 Temporal variability in thermally driven cross-shore exchange: the role of semidiurnal tides. *J. Phys. Oceanogr.* **48** (7), 1513–1531.

Ulloa, H.N., Ramón, C.L., Doda, T., Wüest, A. & Bouffard, D. 2022 Development of overturning circulation in sloping waterbodies due to surface cooling. *J. Fluid Mech.* **930**, A18.

Ulloa, H.N., Winters, K.B., Wüest, A. & Bouffard, D. 2019 Differential heating drives downslope flows that accelerate mixed-layer warming in ice-covered waters. *Geophys. Res. Lett.* **46** (23), 13872–13882.

Wang, X. & Li, Y. 2016 Predicting urban heat island circulation using CFD. *Build. Environ.* **99**, 82–97.

Wedderburn, E.M. 1907 XVI.—The temperature of the fresh-water lochs of Scotland, with special reference to Loch Ness. with appendix containing observations made in Loch Ness by members of the Scottish lake survey. *Trans. R. Soc. Edin.* **45** (2), 407–489.

Wells, M., Griffiths, R. & Turner, J. 1999 Competition between distributed and localized buoyancy fluxes in a confined volume. *J. Fluid Mech.* **391**, 319–336.

Wells, M. & Nadarajah, P. 2009 The intrusion depth of density currents flowing into stratified water bodies. *J. Phys. Oceanogr.* **39** (8), 1935–1947.

Wells, M.G. 2001 Convection, turbulent mixing and salt fingers. PhD thesis, The Australian National University.

Wells, M.G. & Sherman, B. 2001 Stratification produced by surface cooling in lakes with significant shallow regions. *Limnol. Oceanogr.* **46** (7), 1747–1759.

Winters, K.B., Lombard, P.N., Riley, J.J. & D'Asaro, E.A. 1995 Available potential energy and mixing in density-stratified fluids. *J. Fluid Mech.* **289**, 115–128.

Winters, K.B. & Seim, H.E. 2000 The role of dissipation and mixing in exchange flow through a contracting channel. *J. Fluid Mech.* **407**, 265–290.

Winters, K.B. & Young, W.R. 2009 Available potential energy and buoyancy variance in horizontal convection. *J. Fluid Mech.* **629**, 221–230.

Woodward, B., Marti, C., Imberger, J., Hipsey, M. & Oldham, C. 2017 Wind and buoyancy driven horizontal exchange in shallow embayments of a tropical reservoir: Lake Argyle, Western Australia. *Limnol. Oceanogr.* **62** (4), 1636–1657.

Wu, X., Cahl, D. & Voulgaris, G. 2018 Effects of wind stress and surface cooling on cross-shore exchange. *J. Phys. Oceanogr.* **48** (11), 2627–2647.

Wüest, A. & Lorke, A. 2003 Small-scale hydrodynamics in lakes. *Annu. Rev. Fluid Mech.* **35** (1), 373–412.

Yang, B., Young, J., Brown, L. & Wells, M. 2017 High-frequency observations of temperature and dissolved oxygen reveal under-ice convection in a large lake. *Geophys. Res. Lett.* **44**, 12218–12226.

Yu, P., Patterson, J.C. & Lei, C. 2015 A scaling analysis of transient natural convection in a reservoir model induced by iso-flux heating. *J. Fluid Mech.* **764**, 219–249.

Zdorovennova, G. 2009 Spatial and temporal variations of the water–sediment thermal structure in shallow ice-covered Lake Vendyurskoe (Northwestern Russia). *Aquat. Ecol.* **43** (3), 629–639.

Zdorovennova, G., Terzhevik, A., Palshin, N., Efremova, T., Bogdanov, S. & Zdorovennov, R. 2021 Seasonal change in heat flux at the water-bottom sediment boundary in a small lake. *J. Phys.: Conf. Ser.* **2131**, 032080.

Zhang, X. & Nepf, H.M. 2009 Thermally driven exchange flow between open water and an aquatic canopy. *J. Fluid Mech.* **632**, 227–243.

Zhu, D.Z. & Lawrence, G.A. 2001 Holmboe's instability in exchange flows. *J. Fluid Mech.* **429**, 391–409.

Zilitinkevic, S. 1991 *Turbulent Penetrative Convection* (ed. B. Henderson-Sellers). Avebury.

Zilitinkevich, S.S., Kreiman, K.D. & Terzhevik, A.Y. 1992 The thermal bar. *J. Fluid Mech.* **236**, 27–42.

Cite this article: Bouffard D., Doda T., Ramón C.L., Ulloa H.N (2025). Thermally driven cross-shore flows in stratified basins: a review on the thermal siphon dynamics. *Flow*, *5*, E1. doi:10.1017/flo.2024.31